NASA TECHNICAL NOTE

N73-33181

NASA TN D-7269

NASA TN D-7269

ON THE RELATIONSHIP BETWEEN ACOUSTIC ENERGY DENSITY FLUX NEAR THE JET AXIS AND FAR-FIELD ACOUSTIC INTENSITY

by Lucio Maestrello
Langley Research Center
Hampton, Va. 23665

NATIONAL AERONAUTICS AND SPACE ADMINISTRATION • WASHINGTON, D. C. • OCTOBER 1973

1. Report No.
NASA TN D-7269

2. Government Accession No.

3. Recipient's Catalog No.

4. Title and Subtitle
ON THE RELATIONSHIP BETWEEN ACOUSTIC ENERGY DENSITY FLUX NEAR THE JET AXIS AND FAR-FIELD ACOUSTIC INTENSITY

5. Report Date
October 1973

6. Performing Organization Code

7. Author(s)
Lucio Maestrello

8. Performing Organization Report No.
L-8871

9. Performing Organization Name and Address
NASA Langley Research Center
Hampton, Va. 23665

10. Work Unit No.
501-04-01-01

11. Contract or Grant No.

12. Sponsoring Agency Name and Address
National Aeronautics and Space Administration
Washington, D.C. 20546

13. Type of Report and Period Covered
Technical Note

14. Sponsoring Agency Code

15. Supplementary Notes

16. Abstract

By measurement and analysis, the relationship between the distribution of the outflow of acoustic energy over the jet boundary and the far-field intensity is considered. The physical quantity used is the gradient of the pressure evaluated on a geometrical plane at the smallest possible radial distance from the jet axis, but outside the vortical region, in the area where the homogeneous wave equation is reasonably well satisfied. The numerical and experimental procedures involved have been checked out by using a known source. Results indicate that the acoustic power output per unit length of the jet, in the region from which the sound emanates, peaks at approximately 9 diameters downstream. The acoustic emission for a jet Strouhal number of about 0.3 exceeds the emission for all other Strouhal numbers nearly everywhere along the measurement plane. However, the far-field peak intensity distribution obtained from the contribution of each station was found to depend on the spatial extent of the region where sound emanates from the jet, which, in turn, depends more on the far-field angle than on the Strouhal number. For small far-field angles, from the jet axis, the frequency spectrum peak is independent of the Strouhal number, whereas at angles near 90° from the jet axis, it is a weak function of the Strouhal number. These results can also provide guidance on sound suppression by means of surface shielding which can only be achieved when the shielding plane extends beyond 20 nozzle diameters.

17. Key Words (Suggested by Author(s))
Acoustic energy flux
Pressure gradient
Correlation
Far-field intensity
Jet noise

18. Distribution Statement
Unclassified – Unlimited

19. Security Classif. (of this report)
Unclassified

20. Security Classif. (of this page)
Unclassified

21. No. of Pages
62

22. Price*
Domestic, $3.50
Foreign, $6.00

---

*For sale by the National Technical Information Service, Springfield, Virginia 22151

Page Intentionally Left Blank

CONTENTS

SUMMARY 1

INTRODUCTION 1

SYMBOLS 3

THE FLUID FLOW PROBLEM 7
  Analysis 7
  Experimental Setup and Calibration 10
  Flow Measurements 10

THE ACOUSTIC PROBLEM 16
  Analysis 16
  System Calibration 28
  Acoustic Measurements 32

PHOTOGRAPHIC REPRESENTATION OF SOUND FIELD PATTERN EMANATING FROM A JET 36

RESULTS AND DISCUSSION 36
  Evaluation of the Acoustic Energy Density Flux 36
  Evaluation of Far-Field Intensity 42

CONCLUDING REMARKS 47

APPENDIX A – NUMERICAL CALIBRATION FOR THE ACOUSTIC ENERGY FLUX 50

APPENDIX B – DEVELOPMENT AND CALIBRATION OF THE PRESSURE GRADIENT TRANSDUCER 54

REFERENCES 59

ON THE RELATIONSHIP BETWEEN ACOUSTIC ENERGY DENSITY FLUX NEAR THE JET AXIS AND FAR-FIELD ACOUSTIC INTENSITY

By Lucio Maestrello
Langley Research Center

SUMMARY

By measurement and analysis, the relationship between the distribution of the outflow of acoustic energy over the jet boundary and the far-field intensity is considered. The physical quantity used is the gradient of the pressure evaluated on a geometrical plane at the smallest possible radial distance from the jet axis, but outside the vortical region, in the area where the homogeneous wave equation is reasonably well satisfied. The numerical and experimental procedures involved have been checked out by using a known source. Results indicate that the acoustic power output per unit length of the jet, in the region from which the sound emanates, peaks at approximately 9 diameters downstream. The acoustic emission for a jet Strouhal number of about 0.3 exceeds the emission for all other Strouhal numbers nearly everywhere along the measurement plane. However, the far-field peak intensity distribution obtained from the contribution of each station was found to depend on the spatial extent of the region where sound emanates from the jet, which, in turn, depends more on the far-field angle than on the Strouhal number. For small far-field angles, from the jet axis, the frequency spectrum peak is independent of the Strouhal number, whereas at angles near 90° from the jet axis, it is a weak function of the Strouhal number. These results can also provide guidance on sound suppression by means of surface shielding which can only be achieved when the shielding plane extends beyond 20 nozzle diameters.

INTRODUCTION

The problem of jet noise must be formulated in a fashion amenable to experimentation. The direct approach is the evaluation of Lighthill's integral (ref. 1) where the acoustic and the turbulent parts do not appear to be readily separable. During the past 20 years, attempts have been made to evaluate this integral, on the basis of obtaining acoustic far-field information, but it has proved to be a formidable task. An alternative approach, suggested by Maestrello and McDaid (refs. 2 and 3), was to infer as much as possible about the sound generation region of the jet from measurements made outside. This approach has the advantage of simplifying the experimental procedures; however, the simplification is achieved only at the expense of some loss of information. Lilley et al. (ref. 4) follow a theoretical approach similar to that of references 2 and 3 for the sound field radiated from a jet; in addition, they develop a theory for a cyclindrical plug-type flow for the sources in the jet, which has been interpreted as a special case of Doak's unified theory. (See ref. 5.)

The chief objective of the present investigation is to determine the distribution of the acoustic energy density flux out of the jet in terms of the cross correlation of the pressure gradient measured on a geometrical plane outside the vortical region of the jet by following the approach of references 2 and 3. The acoustic energy density flux, although it does not specify exactly the sound generation region of the jet, does determine the zones from which the sound emanates. Furthermore, from the correlation of the pressure gradient on the plane, the far-field acoustic intensity is obtained, in a form which can be seen to be made up of contributions from various zones; thus, the gap between the near-field sound and the far-field sound is bridged.

The approach of this paper presented two potential difficulties: (1) how close can one approach the jet and still remain in the acoustic region? and (2) what is the influence of the entrained flow on the energy flux? To answer these questions, it was necessary to map the velocity field surrounding the jet and to establish the region in which the velocity fluctuations satisfy the homogeneous wave equation.

This approach also permits checking the total acoustic power and the acoustic directivity since both are evaluated by the superposition of the sound field from the various stations along the jet. This verification of the accuracy of the method and of the results is extremely important especially since the method involves making, in effect, radiation field measurements relatively close to the jet; the building of a detailed picture of the sound field as it exits from the jet would thus be permitted, and also the manner in which it is redistributed into the far field can be determined.

In the work reported here, the sound field emanating from an axisymmetric jet has been related to the far-field intensity. In addition, from the measurement of the cross-correlation function of the pressure gradient on the near plane, it has been possible to identify some of the modal features of the sound field emanating from a certain, well-defined conical surface enclosing the jet, this conical surface being defined by wrapping the measurement plane around the jet. This work may help to clarify some of the results obtained in the well-known experimental investigations by Mollo-Christensen (ref. 6) and by Crow and Champagne (ref. 7) who described a wavelike structure of the jet turbulence containing components of all frequencies, the different frequency components preserving their phase relationships over a few diameters. It may also quantify the more recent analytical work of Hardin (ref. 8) in which the source distribution produced by the orderly structure of the turbulence is described. Some other interesting experimental results have been described by Lee and Ribner (ref. 9) which totally differ in principle from those of references 5, 6, and 7, in that the noise sources in a jet are described in terms of point measurements obtained by direct correlations between turbulence and sound; these correlations are not produced by the large-scale orderly structure but by a multi-eddy structure of the flow.

SYMBOLS

A,B	constants (eqs. (B1))
a	longitudinal distance from jet axis to plane
b	radial distance from jet axis to plane
C	constant (eq. (8))
c	speed of sound
D	nozzle diameter
$\vec{f}$	normal stress on surface
f	frequency
f(t)	source strength
$G\left(\vec{r},t \middle\| \vec{r}_o,t_o\right)$	Green's function (eq. (14))
h	source distance from the plane
I(t)	acoustic energy flux
K	pressure gradient transducer sensitivity factor
k	wave number
k_1,k_2,k_3,k_4,k_5	constants

L	longitudinal distance from jet exit
ℓ	longitudinal distance from virtual origin (eq. (8))
P	acoustic power
P_t	total power
p_m	mean pressure
p_o	static pressure
$p(\vec{r},t)$	fluctuating pressure
$p(r)_{rms}$	root-mean-square pressure
R	radial coordinate
R',R''	far-field radial coordinate (eq. (30))
R_{ff}	correlation coefficient for point source strength (eqs. (A5) and (A7))
$R_{V,\nabla p}$	correlation coefficient of normal component of velocity and pressure gradient
$R_{p,p}$	correlation coefficient for far-field sound
$R_{\nabla p,\nabla p}$	correlation coefficient of pressure gradient
$\vec{r}$	position vector for point in space
$\vec{r}_o$	position vector for point on plane
S,S_o	plane areas
S_I	Fourier transform of I (eq. (20))
$S_{V,\nabla p}$	Fourier transform of $R_{V,\nabla p}$ (eq. (22))

$S_{\nabla p,\nabla p}$	Fourier transform of $R_{\nabla p,\nabla p}$
$S(x,t)$	transducer sensitivity
S_{ff}	Fourier transform of R_{ff} (eq. (A7))
S_{rms}	root-mean-square pressure of pressure gradient transducer
$S_{p,p}$	correlation function for far-field intensity
$\mathscr{I}$	far-field intensity
$\mathscr{I}'$	far-field power per unit length of jet
T,t,t_o	time
U_j	jet velocity
u_i,u_j	instantaneous velocities
$\overline{u^2}$	mean square velocity
$\vec{V}$	velocity vector
V_ℓ	longitudinal mean velocity (eq. (10))
V_n	velocity component normal to the plane
V_r	radial mean velocity (eq. (9))
X,Y,Z	Cartesian coordinate system with respect to plane
X_1,Y_1,Z_1	Cartesian coordinate system with respect to nozzle
x_i,x_j	coordinate tensor system
x_o	distance between virtual origin and nozzle exit
α	angle between plane and jet axis (eqs. (37))

α_2	angular relation of plane (eq. (36))
β	far-field angle with respect to nozzle
γ	intermittency factor
δ	delta function (eq. (14))
η	ratio, r/ℓ
θ	far-field angle with respect to plane
ϑ	far-field angle with respect to plane
$\mu(\omega)$	phase angle
ξ	distance between two points in the plane
ρ_m	mean density
ρ_o	static density
$\rho(t)$	fluctuating density
τ	time delay
Φ	velocity potential (eqs. (5) and (8))
ϕ	angle of plane
ψ	mean flow angle (eq. (11))
ω	angular frequency, $2\pi f$
ω'	dummy variable

Primes denote derivatives with respect to variables. Asterisk (*) denotes conjugate and $\langle\ \rangle$ denotes ensemble average.

THE FLUID FLOW PROBLEM

Analysis

Analysis of fluctuating flow outside the jet to determine the position of geometrical measurement plane.- Consider a fluid contained within a half space R bounded by a plane S. When there are no sources of energy within R and no transfer of heat by way of conduction or radiation, the rate of change of energy of the fluid within R is given by the total instantaneous energy flux across the boundary S (that is, the work done on the fluid inside R by the fluid outside R through the action of the surface stresses on S):

$$I(t) = \int_S \left(\vec{f} \cdot \vec{V}\right) dS$$

where $\vec{V}$ and $\vec{f}$ are the fluid velocity and stress at the surface. If a perfect inviscid fluid is assumed, $\left(\vec{f} \cdot \vec{V}\right) dS = pV_n\, dS$, where p is the pressure and V_n is the component of the velocity normal to the plane. The total energy flux then reduces to

$$I(t) = \int_S pV_n\, dS$$

If this expression is to represent only the acoustic energy flux normal to the plane S coming from the jet, the plane must be positioned in a region where the acoustic pressure and fluctuating velocities predominate the mean and turbulent pressures and velocities. To answer the question of how closely one can approach the jet and still remain in the acoustic region, the limit of the region where the wave equation $\left(\text{that is, } \nabla^2 p = \frac{1}{c^2} \frac{\partial^2 p}{\partial t^2}\left[1 + 0\left(10^{-2}\right)\right]\right)$ is reasonably well satisfied must be determined.

This problem can be formulated by considering the basic flow-field equations and observing the behavior of the field in regions near and far from the jet. The continuity and the momentum equations for an inviscid fluid are

$$\left.\begin{aligned} &\frac{\partial \rho}{\partial t} + \frac{\partial}{\partial x_i}\left(\rho u_i\right) = 0 \\ &\rho\left(\frac{\partial u_i}{\partial t} + u_j \frac{\partial u_i}{\partial x_j}\right) + \frac{\partial p}{\partial x_i} = 0 \end{aligned}\right\} \qquad (1)$$

The velocity, pressure, and density are decomposed into static, mean, and fluctuating components:

$$\left.\begin{aligned} u_i &= U_i(\vec{r}) + u_i(\vec{r},t) \\ p &= p_o + p_m(\vec{r}) + p(\vec{r},t) \\ \rho &= \rho_o + \rho_m(\vec{r}) + \rho(\vec{r},t) \end{aligned}\right\} \tag{2}$$

By neglecting quantities of higher order[1] and averaging over time, the mean components can be eliminated to yield

$$\left.\begin{aligned} \frac{\partial\rho(\vec{r},t)}{\partial t} + \rho_o \frac{\partial u_i(\vec{r},t)}{\partial x_i} &= 0 \\ \rho_o \frac{\partial u_i(\vec{r},t)}{\partial t} + \frac{\partial p(\vec{r},t)}{\partial x_i} &= 0 \end{aligned}\right\} \tag{3}$$

for the fluctuating components. It is clear from the second of these two equations that the fluctuating velocity $u_i(\vec{r},t)$ is irrotational. Thus, the fluctuating field described by equations (3) can be called "the irrotational field."

This irrotational field is now divided into two regions: region (1) close to the jet (in terms of acoustic wavelengths) where the velocity fluctuations appropriately normalized by the speed of sound as $u_i(\vec{r},t)/a_o$ are much larger than the relative density fluctuations $\rho(\vec{r},t)/\rho_o$ and thus the fluctuating flow field can be considered incompressible, and region (2) which is further away from the jet where the similarly normalized velocity fluctuations and the density fluctuations are of the same order, that is, $\frac{\rho(\vec{r},t)}{r_o} \propto \frac{u_i(\vec{r},t)}{a_o}$. In region (1) the continuity equation for the fluctuating flow reduces to

$$\rho_o \frac{\partial u_i(\vec{r},t)}{\partial x_i} = 0 \tag{4}$$

By introducing the velocity potential $\vec{u}(\vec{r},t) = \nabla\Phi$, Laplace's equation

$$\nabla^2\Phi = 0 \tag{5}$$

---

[1] Here the perturbations of the mean quantities $U_i(\vec{r})$, $p(\vec{r})$, and $\rho_m(\vec{r})$ have been assumed to be small, as well as the fluctuating perturbations $u_i(\vec{r},t)$, $p(\vec{r},t)$, and $\rho(\vec{r},t)$.

is obtained. In region (2) the density and the pressure fluctuations are related through the isentropic relationship

$$\frac{\partial p(\vec{r},t)}{\partial t} = c^2 \frac{\partial \rho(\vec{r},t)}{\partial t} \tag{6}$$

Again by introducing the velocity potential, the continuity and momentum equations reduce to the wave equation

$$\frac{\partial^2 \Phi}{\partial t^2} - c^2 \nabla^2 \Phi = 0 \tag{7}$$

The region in which the Laplace equation is satisfied has been investigated by O. M. Phillips (ref. 10) and discussed by R. W. Stewart (ref. 11). These references predict a decay of the mean-square fluctuating velocity with the fourth power of the distance from the jet. Measurements by Kibens (ref. 12), Bradbury (ref. 13), and Bradshaw (ref. 14) confirm this prediction. In the region farther away from the jet where the wave equation is applicable, it is well-known that the mean-square velocity decays with the second power of the distance. Hence, by measuring the decay of the mean-square fluctuating velocity, one should be able to determine an optimum position for the plane S at as small as possible distance from the jet boundary. Outside S, of course, the wave equation is then reasonably well satisfied.

Mean flow quantities outside the jet.- By using the same arguments as in the preceding section, it is readily seen that the mean flow in the irrotational region surrounding the jet satisfies Laplace's equation. Stewart (ref. 11) obtained a solution for the velocity potential of this axisymmetric conical mean flow which can be represented as

$$\Phi = -C \log_e\left[\left(\ell^2 + r^2\right)^{1/2} - \ell\right] \tag{8}$$

where C is a positive constant and ℓ and r are the longitudinal and radial distances as measured from the virtual origin of the jet. The radial and longitudinal mean velocity components, V_r and V_ℓ, and the mean flow angle ψ are then

$$V_r = \frac{\partial \Phi}{\partial r} = -\frac{C}{\ell}\frac{1}{\eta}\left[1 + \frac{1}{\left(1+\eta^2\right)^{1/2}}\right] \tag{9}$$

$$V_\ell = \frac{\partial \Phi}{\partial \ell} = \frac{C}{\ell}\frac{1}{\left(1+\eta^2\right)^{1/2}} \tag{10}$$

$$\psi = \text{arc tan}\left(\frac{-V_r}{V_\ell}\right) = \text{arc tan}\left\{\frac{1}{\eta}\left[1 + \left(1 + \eta^2\right)^{1/2}\right]\right\} \qquad (11)$$

where η is the ratio of the radial to the longitudinal distance r/ℓ.

Experimental Setup and Calibration

The position of the plane used to evaluate the acoustic energy density flux along the jet axis was established from a survey of the flow field about the jet. Measurements were made to determine the variation of the mean flow angle and of the mean and fluctuating velocities with distance from the jet boundary.

In order to approximate the ideal situation of a jet expanding into an unbounded and otherwise quiescent region with no mean gradients, the test was set up in a room 10 meters by 10 meters by 30 meters (fig. 1), that is, large enough to insure that the induced flow streamlines were not affected by the walls. The room acted as a huge settling chamber for the induced flow, which passed through a pair of wire damping screens in the upstream section of the room. The nozzle consisted of a long pipe with a diameter of 0.0625 meter connected upstream with an acoustic muffler that acted as a settling chamber for the flow. The flow from the jet was cold and had a mean exit velocity of $U_j = 213$ m/sec.

All the flow measurements were made by use of hot-wire anemometry. Since many of the velocity measurements were extremely low (of the order of 1 m/sec), it was necessary to develop a new procedure for calibrating the hot wire at these low velocities. The rig used, shown in figure 2, consisted of a tube containing a propeller mounted on an essentially frictionless jewel bearing.

By passing known quantities of air through the tube, the frequency of rotation of the propeller was related to the velocity of the air. Then the hot wire was placed in the tube and its output was calibrated against the output of the propeller. To insure reliability of the calibration, the upper velocity range was checked with standard calibration devices at the NASA Langley Research Center and at the National Bureau of Standards.

Flow Measurements

Intermittency.- In order to determine the spreading angle of the flow, the location of the boundary of the jet was established from measurements of the intermittency γ across the jet. The output of the conventional hot-wire anemometers placed in the flow shows irregular bursting of turbulence on a time scale as indicated by figure 3(a). A turbulence detector was used to discriminate between turbulent and nonturbulent flow. The signal was used to give the second time derivative of the velocity $\left|\partial^2 v(t)/\partial t^2\right|$; this value converts into a square wave (fig. 3(b)) and then yields the value of γ, that is, the

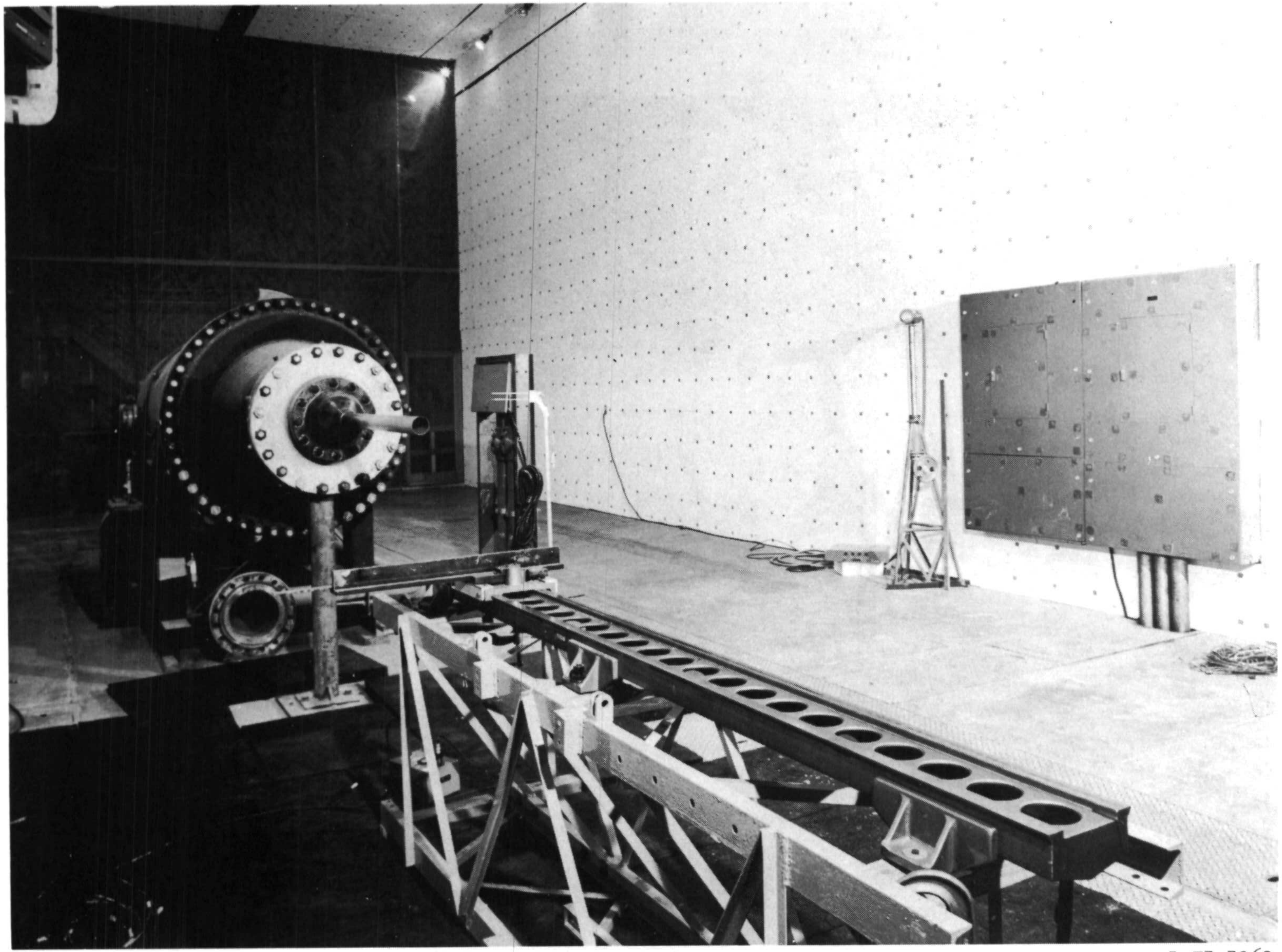

L-73-3069

Figure 1.- Jet noise flow facility.

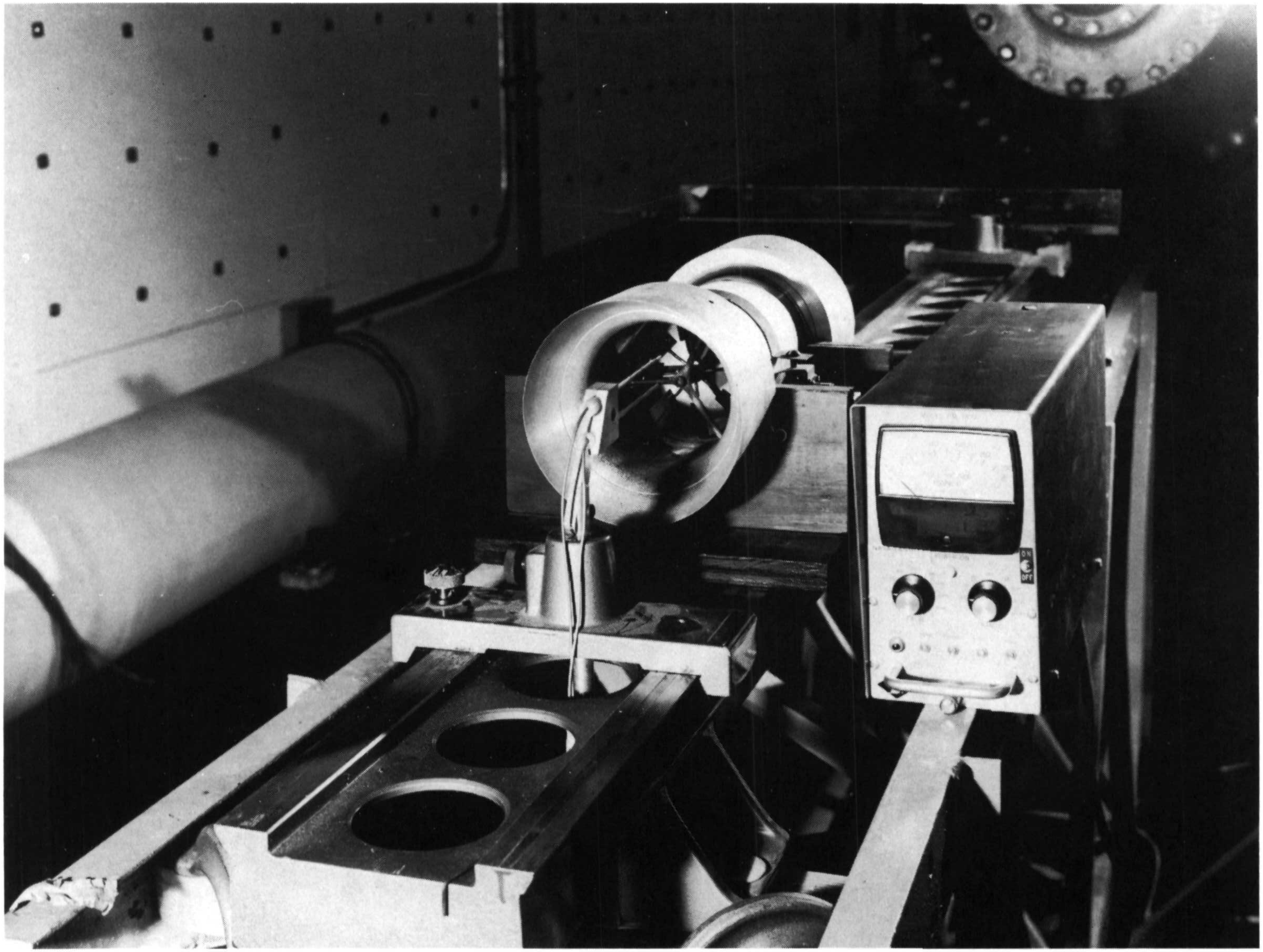

L-73-3070

Figure 2.- Low-velocity hot-wire anemometer calibrator.

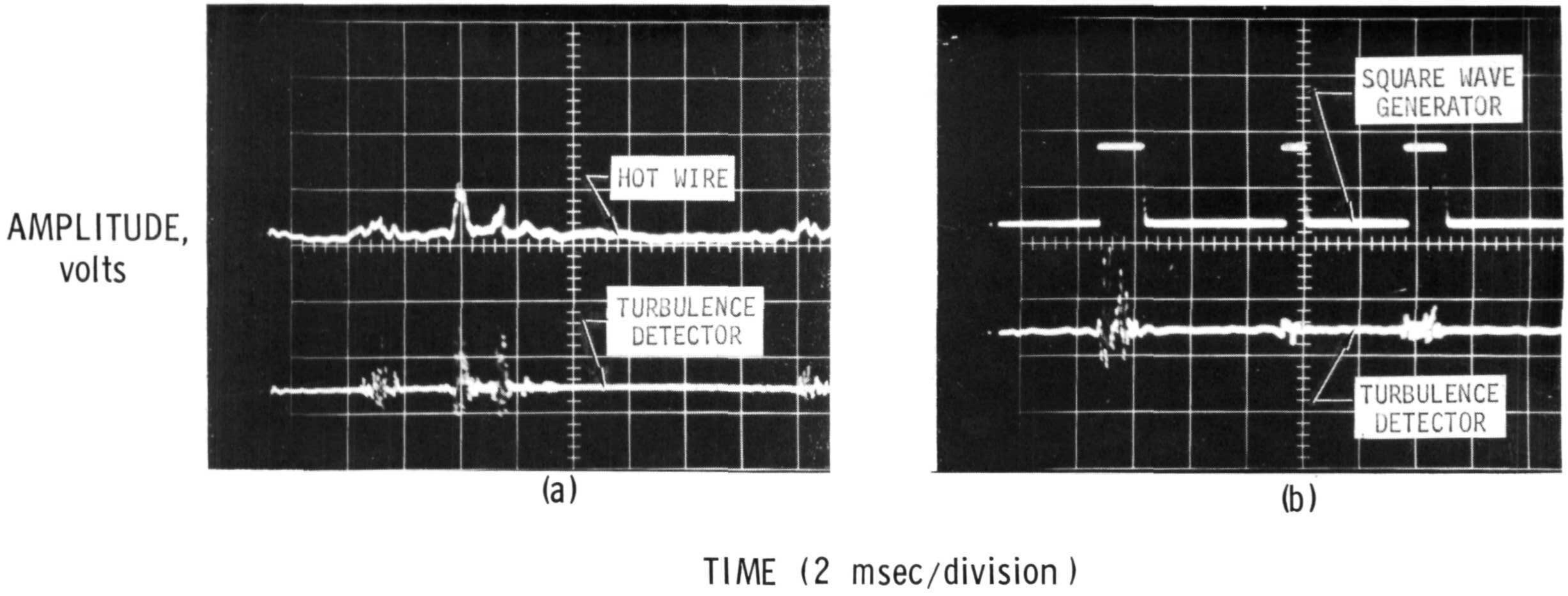

L-73-3071

Figure 3.- Signal conditioning with hot-wire anemometer.

percentage of time that the signal is turbulent. As a result of the large-scale random convolutions of the jet boundary, the value of γ varies smoothly from unity well inside the jet to zero outside the jet.

With the boundary of the jet defined as the position where a particular value of intermittency occurs, the 1-percent and 10-percent boundaries are shown in figure 4.

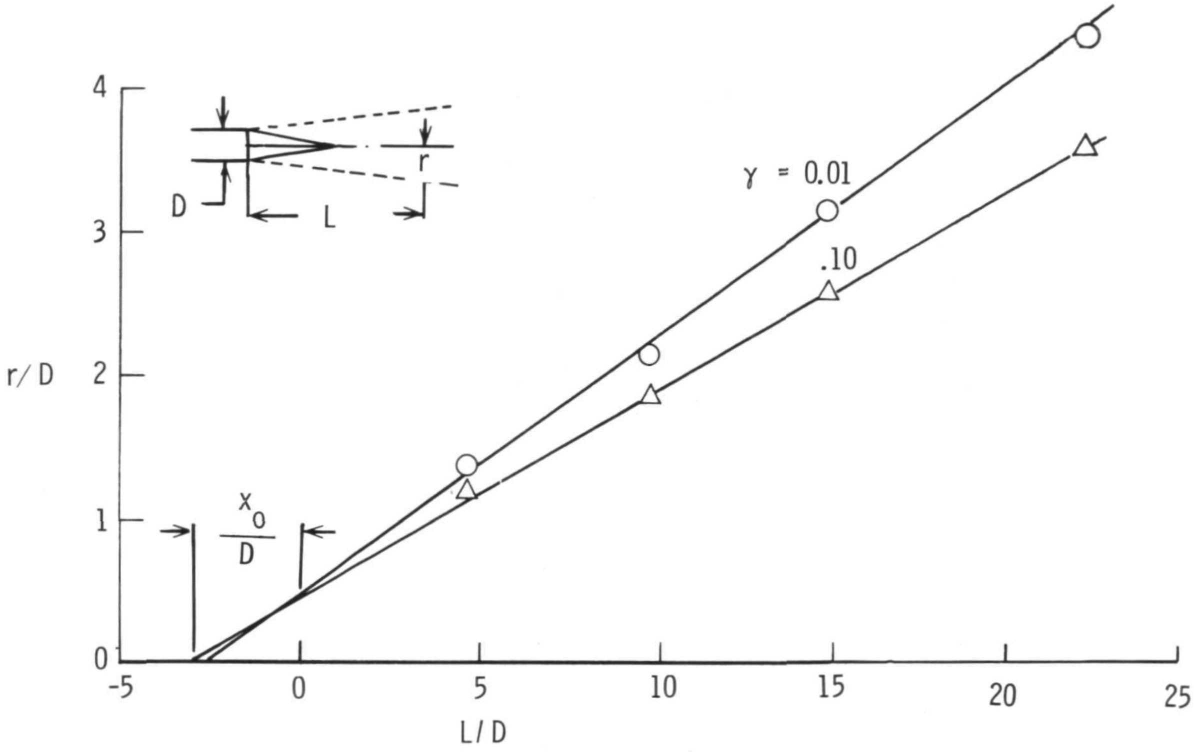

Figure 4.- Jet spreading angle in terms of intermittency distribution.

The figure indicates that the jet spreads at an approximately constant angle, namely, 11° for 1-percent turbulence and 9° for 10-percent turbulence. A virtual origin of the jet, defined as the intersection of the boundary line with the jet center line, is seen to be about 2.5 nozzle diameters upstream of the nozzle exit.

Flow angle.- Measurement of the induced flow angle ψ was made with a pair of cross-wire anemometer probes with a length-diameter ratio of 400:1. Figure 5 shows the results of these measurements at three stations along with intermittency measurements at the furthermost downstream station. It is seen that the flow angle gradually increases as the boundary of the jet is approached from the outside, reaches a maximum in the neighborhood of the boundary, and then quickly decreases to adjust to the direction of the jet.

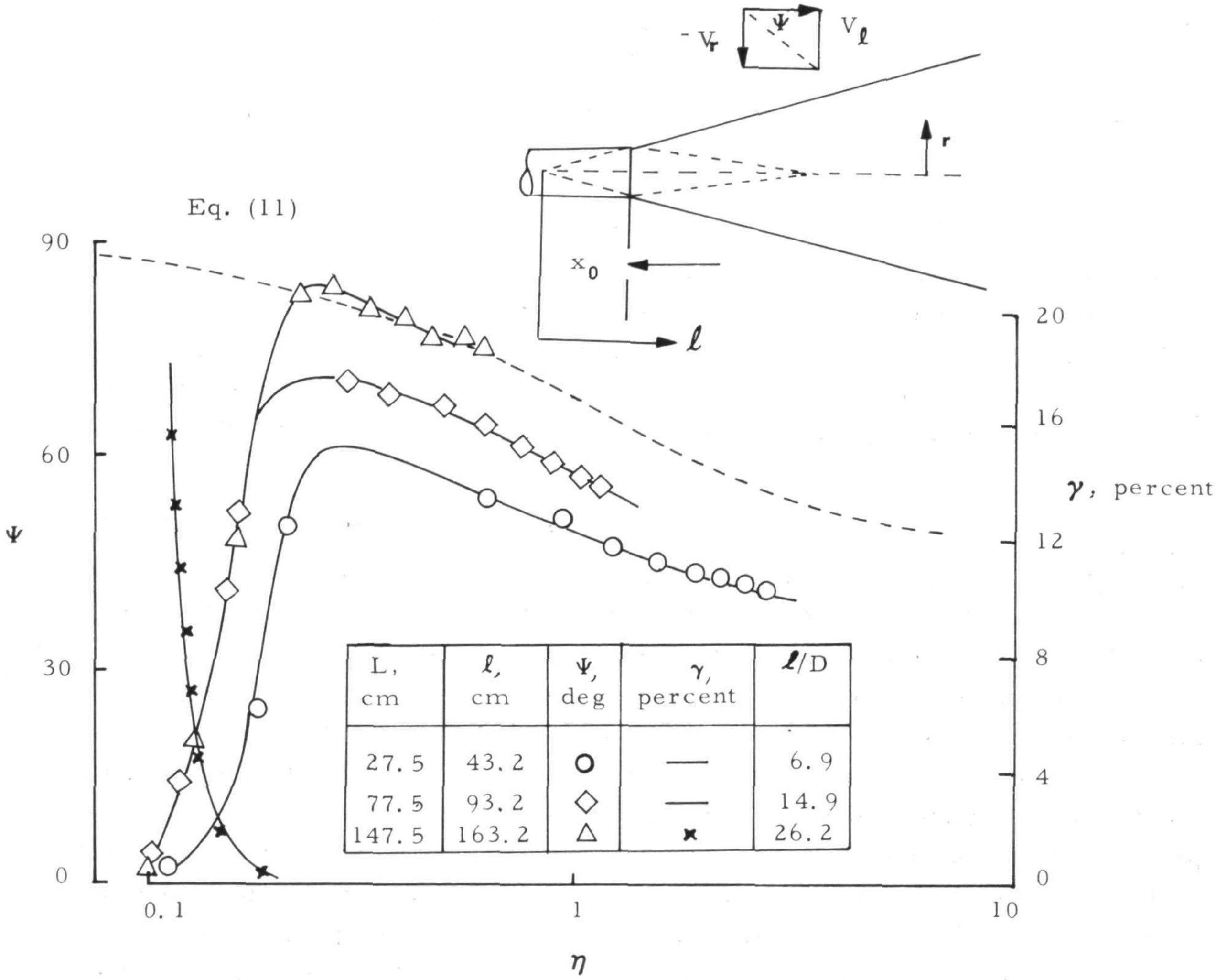

L, cm	ℓ, cm	Ψ, deg	γ, percent	ℓ/D
27.5	43.2	○	—	6.9
77.5	93.2	◇	—	14.9
147.5	163.2	△	×	26.2

Figure 5.- Flow angle and intermittency. $\eta = r/\ell$.

At large distances from the nozzle exit, the maximum flow angle approaches 90°. For this condition the surrounding fluid is entrained into the jet perpendicularly to the jet axis, which implies (ref. 2) that the rate of entrainment remains essentially constant as the jet progresses further downstream. This result conforms with previous measurements (Maestrello and McDaid, ref. 3) and indicates that the entrainment rate increases as the jet moves downstream until it reaches a constant value.

Measurements of the mean flow angle at the furthermost downstream station agree well with those predicted by equation (11), whereas the upstream measurements indicate a smaller angle. (See fig. 5.) This condition is most likely to be caused by the physical boundaries of the flow. The analytical solution is based on flow issuing from a point in unbounded space whereas the experiment has the nozzle and upstream settling chamber interfering with the induced flow. These physical boundaries have less effect further downstream where the analysis and measurements agree.

Mean velocities.- Measurements of the mean radial V_r and mean longitudinal V_ℓ velocity components are shown in figure 6. These measurements are seen to follow equations (9) and (10) at the furthermost downstream station where the constant C is chosen to be 0.43 m^2/sec. Measurements at the other two stations differ from the analysis for the same reasons as the mean flow angle. The variations in the mean velocities at the three stations are similar; most noticeable is the decay of the radial velocity $1/\eta$ with the inverse of the radial distance. The large increase in V_ℓ at small η indicates that these measurements were taken inside the jet boundary. This component will reach a maximum at the jet center line, whereas the radial component V_r will fall off to zero.

Fluctuating velocities.- The measurements of the mean-square fluctuating velocity $\overline{u_1{}^2} + \overline{u_2{}^2} + \overline{u_3{}^2}$ are given in figure 7. As expected from the analysis, two distinct regions are noticed. The first is the incompressible region where the velocity fluctuations obey the Laplace equation and the mean-square velocity decays inversely with the fourth power of the distance. Farther from the jet center line, the mean-square fluctuating velocity decays with the second power of the distance, and thus indicates where the wave equation is applicable. The intersection of these two regions forms a boundary, which can be computed from the figure, and makes an angle of approximately 15° with the jet axis. These results provide information on how close the jet can be approached while still remaining in the acoustic field of the jet. In addition, the influence of the entrainment velocity on the acoustic energy flux will not pose a problem because the mean flow velocity is small and nearly uniform along the plane where the pressure is measured.

THE ACOUSTIC PROBLEM

Analysis

The problem at hand is to express the acoustic energy density flux and the far-field acoustic intensity in terms of the near-field pressure gradient evaluated on an infinite plane at a distance as small as possible from the jet boundary, where the wave equation is reasonably well satisfied. The minimum distance where the acoustic measurements should be made has been established in the preceding sections. The physical quantity to be used in the calculation is the gradient of the pressure, in particular, the measured correlation of this pressure gradient.

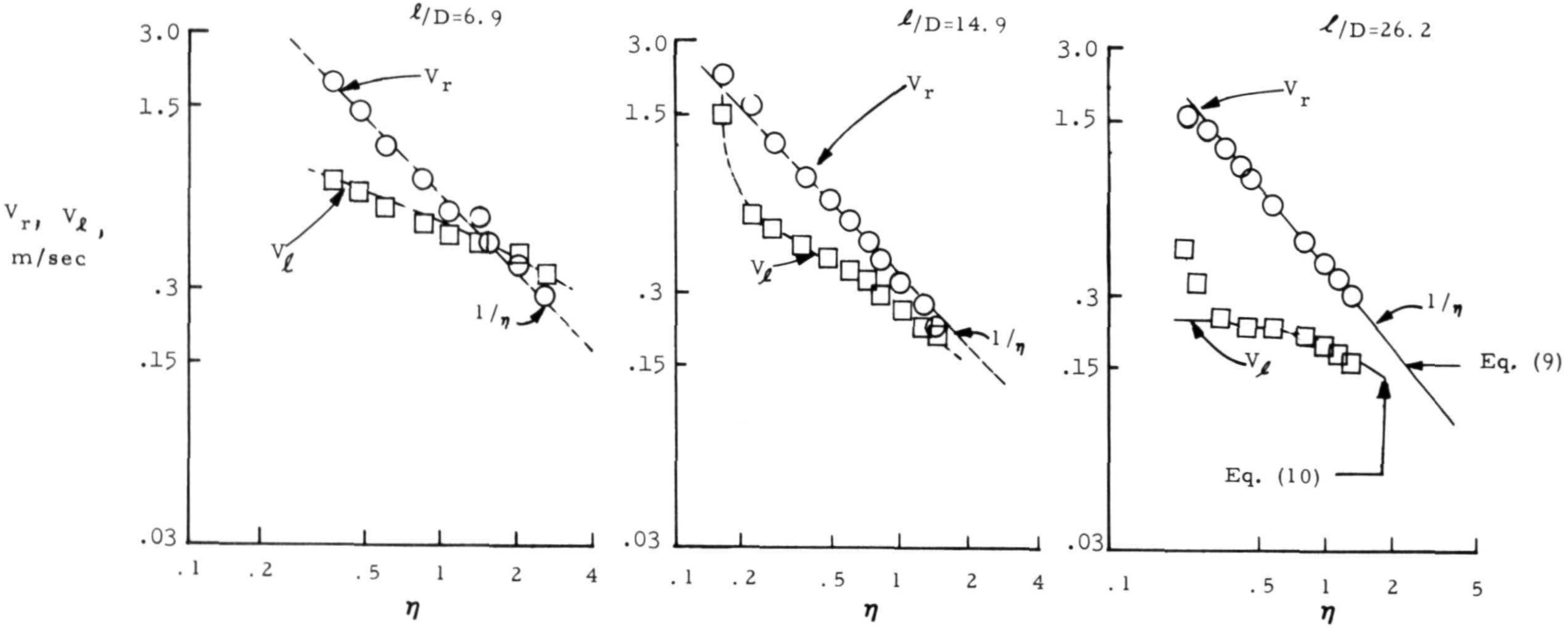

Figure 6.- Mean velocities in irrotational field. $\eta = r/\ell$.

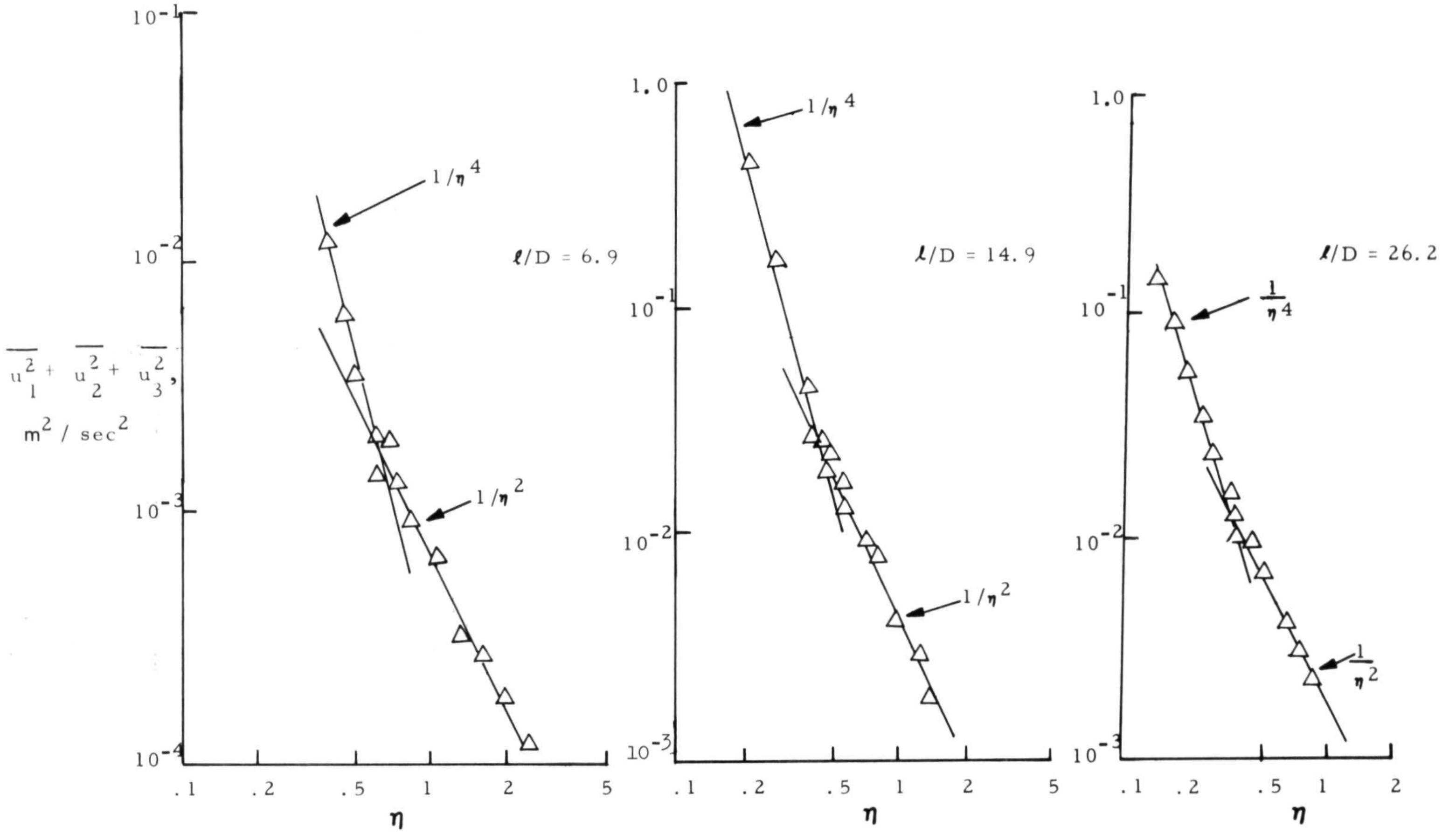

Figure 7.- Fluctuating velocities in irrotational field. $\eta = r/\ell$.

Acoustic energy density flux in terms of the correlation of the pressure gradient on the plane.- The aim is to determine the acoustic energy flux normal to the element of area dS of a plane S inclined at an angle α to the jet axis (fig. 8) in terms of the correlation of the pressure gradient on the plane. The acoustic pressure at any point on or above the plane ($z \geqq 0$) (Morse and Feshbach, ref. 15) satisfies the wave equation and can be expressed as

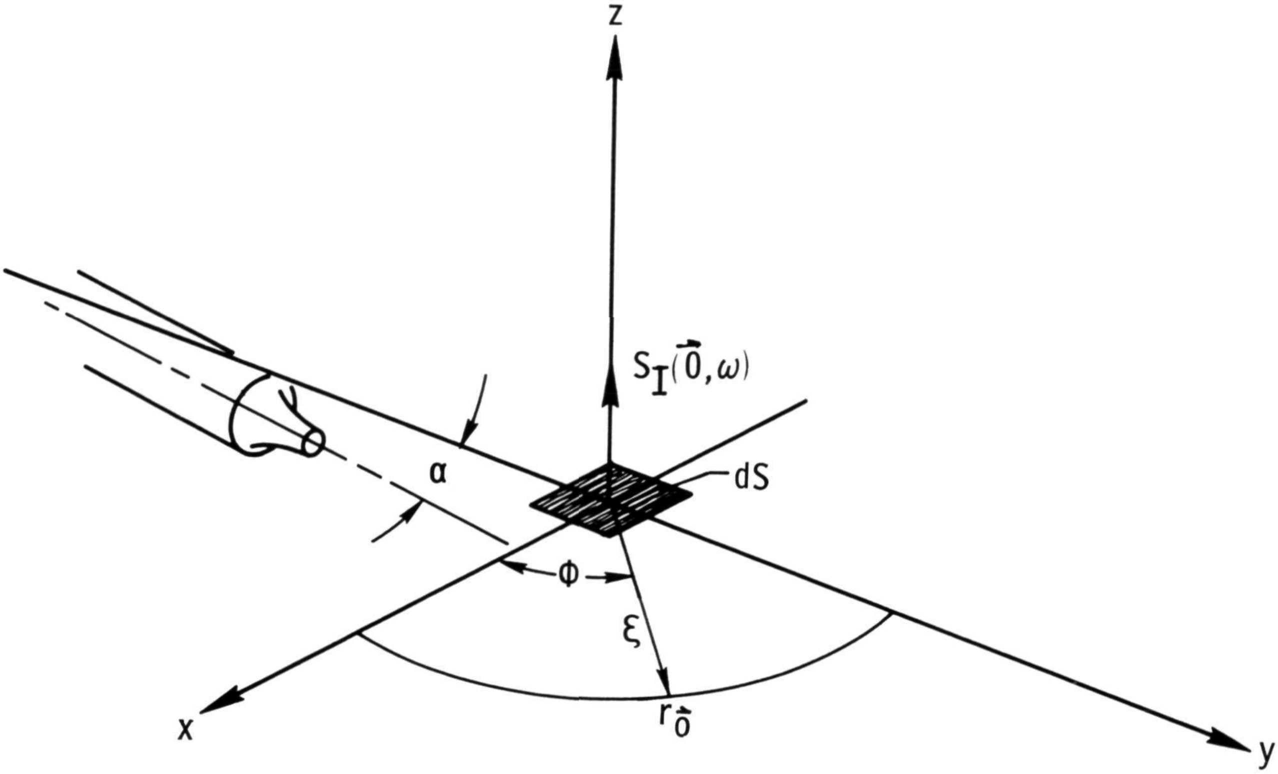

Figure 8.- Coordinate system used in experiment.

$$p(\vec{r},t) = \frac{1}{4\pi}\int_{-\infty}^{t^+} dt_o \int_S dS_o \, G(\vec{r},t|\vec{r}_o,t_o)\frac{\partial p(\vec{r}_o,t)}{\partial z} \tag{12}$$

where the Green's function G satisfies the conditions

$$\left(\nabla^2 - \frac{1}{c^2}\frac{\partial^2}{\partial t^2}\right)G = -4\pi\delta(\vec{r} - \vec{r}_o)\delta(t - t_o)$$

$$\frac{\partial G}{\partial z} = 0 \qquad \text{(on S)} \tag{13}$$

The solution for the Green's function is known to be

$$G\left(\vec{r},t\middle|\vec{r}_o,t_o\right) = \frac{2\delta\left[\frac{R}{c} - \left(t - t_o\right)\right]}{R} = \frac{1}{\pi R}\int_{-\infty}^{\infty} d\omega' e^{-i\omega'\frac{R}{c}} e^{-i\omega'\left(t_o - t\right)} \tag{14}$$

where δ is the Dirac delta function and $R = \left|\vec{r} - \vec{r}_o\right|$. Hence the acoustic pressure on and above the plane is given by

$$p\left(\vec{r},t\right) = \frac{1}{4\pi^2}\int_{-\infty}^{0^+} dt_1 \int_S \frac{dS_o}{R}\int_{-\infty}^{\infty} d\omega' e^{-i\omega'\frac{R}{c}} e^{-i\omega' t_1} \frac{\partial p\left(\vec{r}_o,\, t+t_1\right)}{\partial z} \tag{15}$$

where

$$t_1 = t_o - t$$

A generalized complex acoustic intensity in the n direction[2] whose real part represents, when $\tau = 0$, the normal component of the acoustic energy flux can be defined as

$$I\left(\vec{r},\tau\right) = \left\langle p\left(\vec{r},t\right) V_n^*\left(\vec{r},\, t+\tau\right)\right\rangle \tag{16}$$

By substituting the pressure from equation (15) into equation (16), the intensity becomes

$$I\left(\vec{r};\tau\right) = \frac{1}{4\pi^2}\int_{-\infty}^{0^+} dt_1 \int_S \frac{dS_o}{R}\int_{-\infty}^{\infty} d\omega' e^{-i\omega'\frac{R}{c}} e^{-i\omega' t_1}\left\langle V_n\left(\vec{r},\, t+\tau\right)\frac{\partial p\left(\vec{r}_o,\, t+t_1\right)}{\partial z}\right\rangle \tag{17}$$

since

$$\left\langle V_n^*\left(\vec{r},\, t+\tau\right)\frac{\partial p\left(\vec{r}_o,\, t+t_1\right)}{\partial z}\right\rangle = \left\langle V_n^*\left(\vec{r};\, \left[t+t_1\right]+\left[\tau-t_1\right]\right)\frac{\partial p\left(\vec{r}_o,\, t+t_1\right)}{\partial z}\right\rangle \tag{18}$$

By introducing the correlation coefficient between velocity and the pressure gradient, and on the basis of stationarity, one can show that

---

[2] This generalized intensity which evidently is a correlation function of pressure with velocity is convenient when the subsequent equations are to be expressed in terms of correlations.

$$R_{V,\nabla p}(\vec{r},\vec{r}_o;\tau) \equiv \left\langle V_z^*(\vec{r},\, t+\tau)\frac{\partial p}{\partial z}(\vec{r}_o,t)\right\rangle \equiv \lim_{T\to\infty} \frac{1}{2T}\int_{-T}^{T} V_z^*(\vec{r},\, t+\tau)\frac{\partial p}{\partial z}(\vec{r}_o,t)\, dt$$

Therefore

$$\left\langle V_z^*\left[\vec{r}(t + t_1) + (\tau - t_1)\right]\frac{\partial p(\vec{r}_o,\, t+t_1)}{\partial z}\right\rangle = R_{V,\nabla p}(\vec{r},\vec{r}_o;\, \tau-t_1) \tag{19}$$

Taking the Fourier transform of equation (17) yields

$$\begin{aligned} S_I(\vec{r};\omega) &= \int_{-\infty}^{\infty} I(\vec{r},\tau)e^{-i\omega\tau}\, d\tau \\ &= \frac{1}{4\pi^2}\int_{-\infty}^{0^+} dt_1 \int_S \frac{dS_o}{R}\int_{-\infty}^{\infty} d\omega' \int_{-\infty}^{\infty} d\tau\, e^{-i\omega\tau} e^{-i\omega'\frac{R}{c}} e^{-i\omega' t_1} R_{V,\nabla p}(\vec{r},\vec{r}_o;\, \tau-t_1) \end{aligned} \tag{20}$$

Upon changing the variables of integration with the transformation

$$t' = t_1$$

$$t'' = \tau - t_1$$

equation (19) becomes

$$\begin{aligned} S_I(\vec{r};\omega) &= \frac{1}{4\pi^2}\int_S \frac{dS_o}{R}\int_{-\infty}^{0^+} dt' e^{-i\omega t'} \int_{-\infty}^{\infty} d\omega' e^{-i\omega'\left(\frac{R}{c}+t'\right)} \int_{-\infty}^{\infty} dt''\, e^{-i\omega t''} R_{V,\nabla p}(\vec{r},\vec{r}_o;t'') \\ &= \frac{1}{4\pi^2}\int_S \frac{dS_o}{R}\int_{-\infty}^{0^+} dt' e^{-i\omega t'} 2\pi\delta\left(\frac{R}{c} + t'\right) S_{V,\nabla p}(\vec{r},\vec{r}_o;\omega) \\ &= \frac{1}{2\pi}\int_S \frac{dS_o}{R}\, e^{i\omega\frac{R}{c}} S_{V,\nabla p}(\vec{r},\vec{r}_o;\omega) \end{aligned} \tag{21}$$

where

$$S_{V,\nabla p}(\vec{r},\vec{r}_o;\omega) \equiv \int_{-\infty}^{\infty} dt\, e^{-i\omega t} R_{V,\nabla p}(\vec{r},\vec{r}_o;t) \tag{22}$$

The experiments as discussed earlier yield the correlation of pressure gradient with a pressure gradient rather than its correlation with velocity. It can be shown with the use of the equation of motion that these two correlations are related by

$$\left.\begin{aligned}
&\frac{\partial}{\partial\tau} R_{V,\nabla p}\left(\vec{r},\vec{r}_o;\tau\right) = \frac{1}{\rho} R_{\nabla p,\nabla p}\left(\vec{r},\vec{r}_o;\tau\right) \\
&\left\langle \frac{\partial V_z^{*}\left(\vec{r},t\right)}{\partial t} \, \frac{\partial p\left(\vec{r}_o,\, t+\tau\right)}{\partial z} \right\rangle = \lim_{T\to\infty} \frac{1}{2T} \int_{-T}^{T} \frac{\partial V_z^{*}\left(\vec{r},t\right)}{\partial t} \, \frac{\partial p\left(\vec{r}_o,\, t+\tau\right)}{\partial z} \, dt \\
&\qquad = \lim_{T\to\infty} \frac{1}{2T} \int_{-T}^{T} \frac{\partial}{\partial t}\left[V_z^{*}\left(\vec{r},t\right) \frac{\partial p\left(\vec{r}_o,\, t+\tau\right)}{\partial z}\right] - \frac{V_z^{*}\left(\vec{r},t\right)\, \partial^2 p\left(\vec{r}_o,\, t+\tau\right)}{\partial t\, \partial z} \, dt \\
&\qquad = \frac{\partial}{\partial\tau}\left[\lim_{T\to\infty} \frac{1}{2T} \int_{-T}^{T} V_z^{*}\left(\vec{r},t\right) \frac{\partial p\left(\vec{r}_o,\, t+\tau\right)}{\partial z} \, dt\right] \\
&\qquad = -\frac{\partial}{\partial\tau} R_{V,\nabla p}\left(\vec{r},\vec{r}_o;\tau\right)
\end{aligned}\right\} \tag{23a}$$

since

$$\left.\begin{aligned}
&\left\langle \frac{\partial V^{*}\left(\vec{r},t\right)}{\partial t} \, \frac{\partial p\left(\vec{r}_o,\, t+\tau\right)}{\partial z} \right\rangle = \frac{1}{\rho} \left\langle \frac{\partial p^{*}\left(\vec{r},t\right)}{\partial z} \, \frac{\partial p\left(\vec{r}_o,\, t+\tau\right)}{\partial z} \right\rangle \\
&\frac{1}{\rho} R_{\nabla p,\nabla p}\left(\vec{r},\vec{r}_o;\tau\right) = -\frac{\partial}{\partial\tau} R_{V,\nabla p}\left(\vec{r},\vec{r}_o;\tau\right)
\end{aligned}\right\} \tag{23b}$$

where

$$R_{\nabla p,\nabla p}\left(\vec{r},\vec{r}_o;\tau\right) \equiv \left\langle \frac{\partial p^{*}\left(\vec{r},\, t+\tau\right)}{\partial z} \, \frac{\partial p\left(\vec{r}_o,t\right)}{\partial z} \right\rangle \tag{24}$$

By taking the Fourier transform of equations (23a) and integrating the left-hand side, one obtains

$$S_{V,\nabla p}\left(\vec{r},\vec{r}_o;\omega\right) = \frac{1}{i\omega\rho} S_{\nabla p,\nabla p}\left(\vec{r},\vec{r}_o;\omega\right) \tag{25}$$

where

$$S_{\nabla p,\nabla p}\left(\vec{r},\vec{r}_o;\omega\right) \equiv \int_{-\infty}^{\infty} d\tau\, e^{-i\omega\tau} R_{\nabla p,\nabla p}\left(\vec{r},\vec{r}_o;\tau\right) \tag{26}$$

Hence equation (21) becomes

$$S_I\left(\vec{r};\omega\right) = \frac{1}{2\pi i\omega\rho} \int_S dS_o \, \frac{e^{i\omega\frac{R}{c}}}{R} \, S_{\nabla p,\nabla p}\left(\vec{r},\vec{r}_o;\omega\right) \tag{27}$$

Since the acoustic energy density flux through the plane is the main concern, $\vec{r}$ will be a point on the plane which, for convenience, may be chosen to be the origin of the coordinate system. In terms of polar coordinates ξ, ϕ in the plane, equation (27) becomes

$$S_I(0;\omega) = \frac{1}{2\pi i\omega\rho} \int_0^{2\pi} d\phi \int_0^{\infty} d\xi \, e^{i\omega\frac{\xi}{c}} S_{\nabla p, \nabla p}(0, \xi, \phi; \omega) \tag{28}$$

where

$$S_{\nabla p, \nabla p}(0, \xi, \phi, \omega) \equiv S_{\nabla p, \nabla p}\left(\vec{0}, \vec{r}_o; \omega\right)$$

The total power per unit length of the jet crossing the plane S is obtained by an integration of the area elements dS around the jet. Since the jet is axially symmetric,

$$\frac{P}{dx} = 2\pi b \int_0^{\infty} S_I(0;\omega) \, d\omega$$

where b is the radial distance from the jet axis to the plane. To show that equation (28) yields a correct analytical result, consider for the case of a monopole of strength f(t) located directly below the origin at $z = -h$. This case provides a numerical calibration of the method. The solution for the Fourier transform of the acoustic intensity from equation (28) is given in appendix A as equation (A8).

$$S_I\left(\vec{0};\omega\right) = \frac{\left(1 + i\frac{\omega}{c}h\right)e^{-i\frac{\omega h}{c}} S_{ff}(\omega)}{i\omega\rho h} \int_0^{\infty} d\xi \frac{\left[1 - i\frac{\omega}{c}\left(\xi^2 + h^2\right)^{1/2}\right] e^{i\frac{\omega}{c}\left[\left(\xi^2 + h^2\right)^{1/2} + \xi\right]}}{\left(\xi^2 + h^2\right)^{3/2}}$$

This solution should equal the answer obtained by direct means (eq. (A9))

$$S_I\left(\vec{0};\omega\right) = \left(1 + i\frac{c}{\omega h}\right)\frac{S_{ff}(\omega)}{\rho c h^2}$$

Far-field intensity from correlation on the plane.- The far-field intensity will now be determined from measurements of the cross spectral density $S_{\nabla p, \nabla p}\left(\vec{0}, \vec{r}_o; \omega\right)$ on the plane S. Since there are no sources in the volume above the plane, the far-field pressure is given by equation (12) which can be written as

$$p(\vec{r},t) = \frac{1}{4\pi^2}\int_{-\infty}^{t^+} dt_o \int_S dS_o \int_{-\infty}^{\infty} d\omega' e^{i\omega'(t-t_o)} \frac{e^{-i\omega'\frac{R}{c}}}{R} \frac{\partial p(\vec{r}_o,t_o)}{\partial z} \tag{29}$$

where $R = \left|\vec{r} - \vec{r}_o\right|$, $\vec{r}_o$ is on the plane, and $\vec{r}$ is the far-field point as shown in figure 9. The cross correlation of the pressure at $\vec{r}$ is

$$\begin{aligned} R_{p,p}(\vec{r};\tau) &= \left\langle p(\vec{r},t)\ p^*(\vec{r},\ t+\tau)\right\rangle \\ &= \frac{1}{16\pi^4}\int_{-\infty}^{t^+} dt_o' \int_{-\infty}^{t^++\tau} dt_o'' \int_S dS_o' \int_S dS_o'' \int_{-\infty}^{\infty} d\omega' \int_{-\infty}^{\infty} d\omega''\ e^{i\omega'(t-t_o')}\ e^{-i\omega''(t-t_o'')} \frac{e^{-i\frac{\omega'}{c}R'}}{R'} \frac{e^{i\frac{\omega''}{c}R''}}{R''} R_{\nabla p,\nabla p}\left(\vec{r}_o',\vec{r}_o'',\ t_o''-t_o'\right) \end{aligned} \tag{30}$$

where

$$R_{\nabla p,\nabla p}\left(\vec{r}_o',\vec{r}_o'',\ t_o''-t_o'\right) = \left\langle \frac{\partial p(\vec{r}_o',t_o')}{\partial z}\ \frac{\partial p^*(\vec{r}_o'',t_o'')}{\partial z} \right\rangle$$

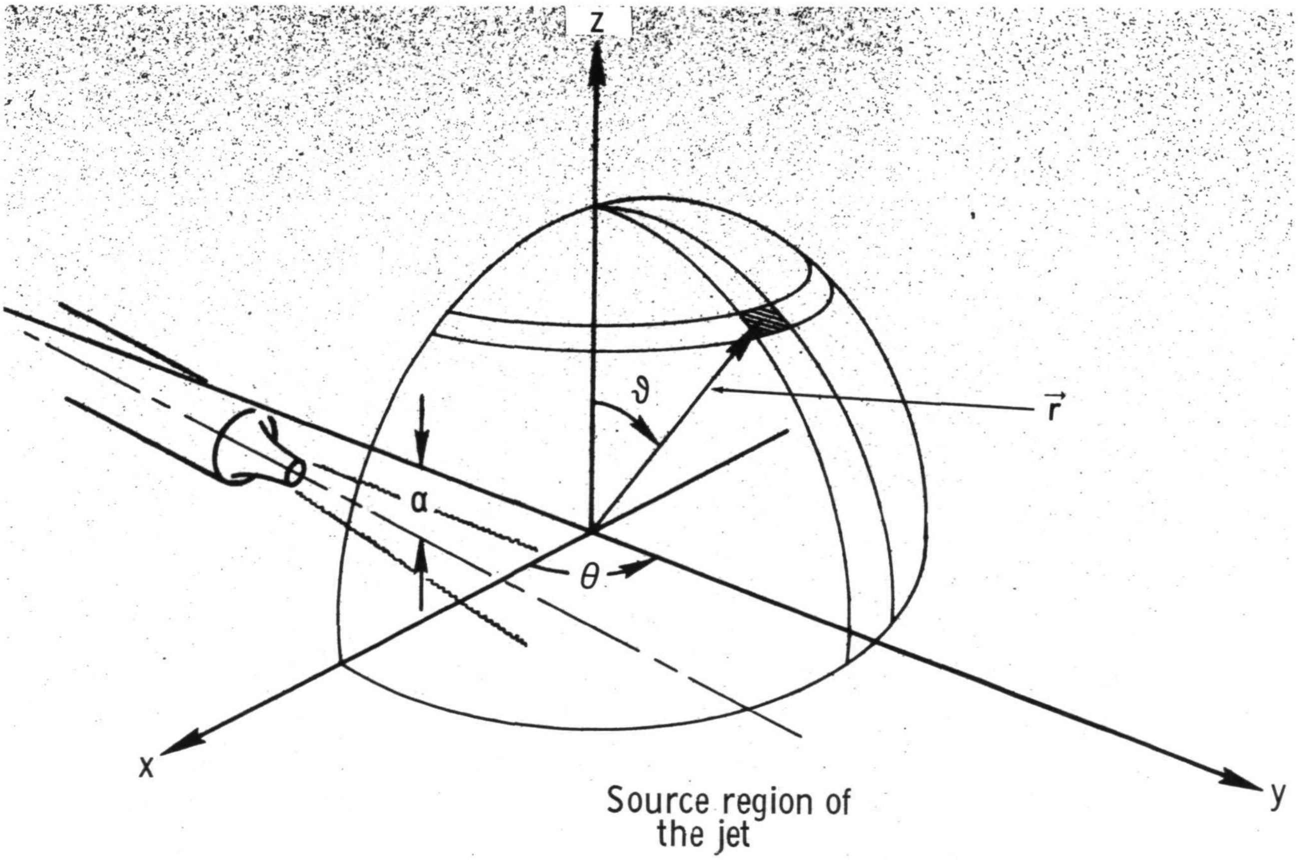

Figure 9.- Far-field geometry for calculation of the intensity. $dA = (r \sin \vartheta\ d\theta)(r\ d\vartheta)$.

Without any further loss of generality, one might let $t = 0$ and introduce $t_o = t_o'' - \tau$; then the spectral density of the mean-square pressure at $\vec{r}$ is

$$S_{p,p}(\vec{r};\omega) = \int_{-\infty}^{\infty} d\tau\, e^{-i\omega\tau} R_{p,p}(\vec{r};\tau)$$

$$= \frac{1}{16\pi^4} \int_{-\infty}^{\infty} d\tau \int_{-\infty}^{0^+} dt_o' \int_{-\infty}^{0^+} dt_o'' \int_S dS_o' \int_S dS_o'' \int_{-\infty}^{\infty} d\omega' \int_{-\infty}^{\infty} d\omega''\, e^{-i\omega\tau} \frac{e^{-i\omega'\left(t_o' + \frac{R'}{c}\right)}}{R'} \frac{e^{i\omega''\left(t_o + \frac{R''}{c}\right)}}{R''} R_{\nabla p, \nabla p}\left(\vec{r}_o', \vec{r}_o''; \tau + t_o - t_o'\right) \tag{31}$$

Changing the variables of integration by transforming

$$t_1 = t_o$$

$$t_2 = t_o'$$

$$t_3 = \tau + t_o - t_o'$$

yields

$$S_{p,p}(\vec{r};\omega) = \frac{1}{16\pi^4} \int_{-\infty}^{\infty} dt_3 \int_{-\infty}^{\infty} dt_2 \int_{-\infty}^{\infty} dt_1 \int_S dS_o' \frac{e^{-i\omega(t_3 - t_1 + t_2)}}{R'R''} R_{\nabla p, \nabla p}\left(\vec{r}_o', \vec{r}_o''; t_3\right) \int_{-\infty}^{\infty} d\omega'\, e^{i\omega'\left(t_2 + \frac{R'}{c}\right)} \int_{-\infty}^{\infty} d\omega''\, e^{i\omega''\left(t_1 + \frac{R''}{c}\right)}$$

$$= \frac{1}{4\pi^2} \int_{-\infty}^{\infty} dt_3 \int_{-\infty}^{0^+} dt_2 \int_{-\infty}^{0^+} dt_1 \int_S dS_o' \int_S dS_o'' \frac{e^{-i\omega t_3}\, e^{i\omega t_1}\, e^{-i\omega t_2}}{R'R''} R_{\nabla p, \nabla p}\left(\vec{r}_o', \vec{r}_o'', t_3\right) \delta\left(t_2 + \frac{R'}{c}\right) \delta\left(t_1 + \frac{R''}{c}\right)$$

which reduces to

$$S_{p,p}(\vec{r}, \omega) = \frac{1}{4\pi^2} \int_S \int_S dS_o'\, dS_o'' \frac{e^{-i\frac{\omega}{c}R''}}{R''} \frac{e^{i\frac{\omega}{c}R'}}{R'} S_{\nabla p, \nabla p}\left(\vec{r}_o', \vec{r}_o''; \omega\right) \tag{32}$$

where

$$S_{\nabla p, \nabla p}\left(\vec{r}_o', \vec{r}_o''; \omega\right) = \int_{-\infty}^{\infty} d\tau\, e^{-i\omega\tau} R_{\nabla p, \nabla p}\left(\vec{r}_o', \vec{r}_o''; \tau\right)$$

Now consider $\vec{r}$ to be the far-field point shown in figure 9 and express it in terms of the spherical coordinates r, ϑ, θ. Thus,

$$R' = r\left[1 - \frac{\sin \vartheta}{r}(x' \cos \theta + y' \sin \theta) + O\left(\frac{1}{r^2}\right)\right]$$

and

$$\lim_{r\to\infty} r^2 \frac{e^{i\frac{\omega}{c}R'}}{R'} \frac{e^{-i\frac{\omega}{c}R''}}{R''} = e^{i\frac{\omega}{c}\sin\vartheta\left[(x''-x')\cos\theta+(y''-y')\sin\theta\right]}$$

As a result, the spectral density of the mean-square pressure at the far-field point $\vec{r}$ becomes

$$S_{p,p}(r,\theta,\vartheta;\omega) = \frac{1}{4\pi^2}\iint_{-\infty}^{\infty} dx'\,dy' \iint_{-\infty}^{\infty} dx''\,dy''\, S_{\nabla p,\nabla p}\left(\vec{r}_o{}',\vec{r}_o{}'';\omega\right) \frac{e^{i\frac{\omega}{c}\sin\vartheta\left[(x''-x')\cos\theta+(y''-y')\sin\theta\right]}}{r^2} \qquad (33)$$

One can calculate the contribution $\mathscr{S}$ to the far-field spectral density of the pressure coming from the point $\vec{r}_o$ which, for convenience, is chosen to be the origin. Define

$$S_{p,p}(r,\theta,\vartheta;\omega) = \iint_{-\infty}^{\infty} dx'\,dy'\,\mathscr{S}\left(r,\theta,\vartheta,\vec{r}_o{}';\omega\right) \qquad (34)$$

By using the notation of figure 8, that is,

$$x'' - x' = \xi\cos\phi$$

$$y'' - y' = \xi\sin\phi$$

one obtains from equation (33)

$$(2\pi r)^2\mathscr{S}\left(r,\theta,\vartheta,\vec{0};\omega\right) = \int_0^{2\pi} d\phi \int_0^{\infty} \xi\,d\xi\, e^{i\frac{\omega}{c}\xi\sin\vartheta\cos(\phi-\theta)} S_{\nabla p,\nabla p}\left(\vec{0},\xi,\phi;\omega\right) \qquad (35)$$

In effect, the far-field spectral density has been replaced by a sum of contributions from apparent sources at each point on the plane S. It is of more interest to calculate the far field in term of contributions per unit length of the jet. Since the correlation distribution is the same at each circumferential point of an axisymmetric jet, the plane appears to be rotated about the jet to form a conical surface wrapped around the jet. By referring to the notation of figure 10, the contribution to the spectral density of the mean-square pressure at the far-field point R,β coming from the conical strip at $x_1 = a$ can be formulated as

$$\mathscr{S}'(R,\beta;\omega,\Delta x) = \int_{\text{Strip}} \mathscr{S}\left(r,\theta,\vartheta,\vec{0};\omega\right) d\alpha_2 \qquad (36)$$

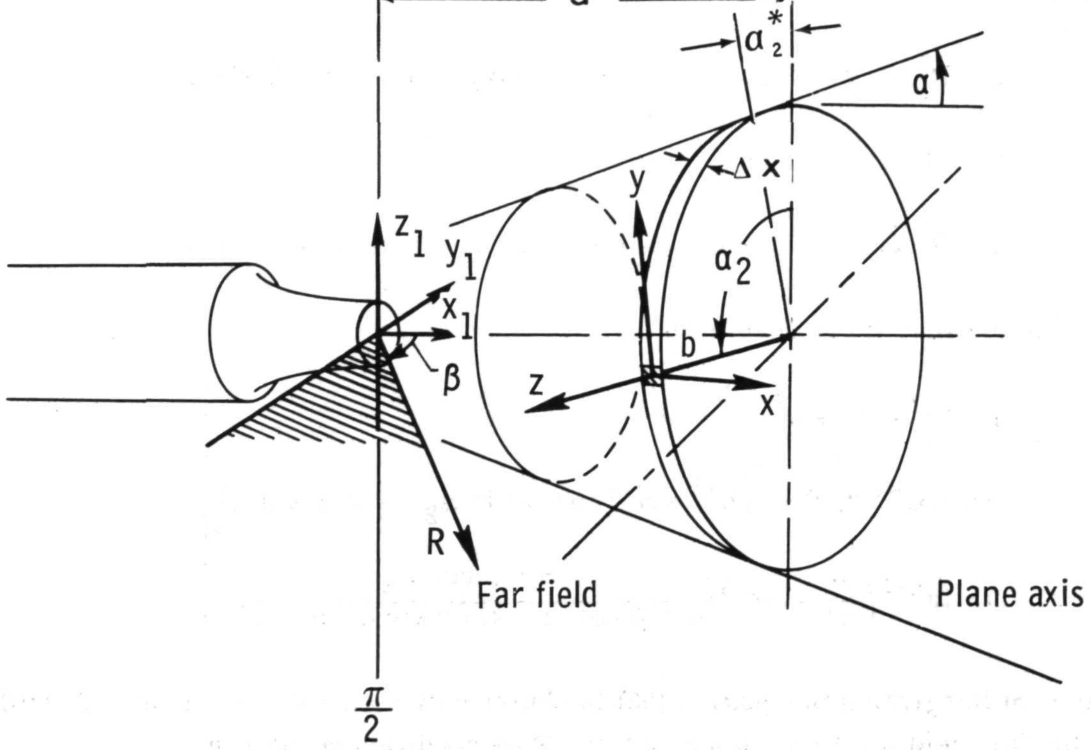

Figure 10.- Far-field geometry used for determining the power per unit length.

It now remains to express the far-field coordinates with respect to the plane r, θ, ϑ in terms of the far-field coordinates with respect to the jet R, β and the angle α_2 at which the plane is rotated. The Cartesian transformation between the two far-field coordinate systems is obtained by simple translation and rotations as

$$x = \left(x_1 - a\right)\cos \alpha + \left(z_1 \cos \alpha_2 - y_1 \sin \alpha_2 - b\right)\sin \alpha$$

$$y = y_1 \cos \alpha_2 + b \sin \alpha_2 \cos \alpha_2 + z_1 \sin \alpha_2 \cos \alpha_2$$

$$z = -\left(x_1 - a\right)\sin \alpha + \left(z_1 \cos \alpha_2 - y_1 \sin \alpha_2 - b\right)\cos \alpha$$

By noting that for the far-field point of interest,

$$x_1 = R \cos \beta$$

$$y_2 = -R \sin \beta$$

$$z_1 = 0$$

one obtains

$$x = R\left(\cos \beta \cos \alpha + \sin \beta \sin \alpha \sin \alpha_2\right) - a \cos \alpha - b \sin \alpha$$

$$y = -R\left(\sin \beta \cos \alpha_2\right)$$

$$z = R\left(\sin \beta \cos \alpha \sin \alpha_2 - \cos \beta \sin \alpha\right) + a \sin \alpha - b \cos \alpha$$

Letting R become large results in

$$\left.\begin{aligned} r &= \left(x^2 + y^2 + z^2\right)^{1/2} = R \\ \vartheta &= \cos^{-1}(z/r) = \cos^{-1}\left(\sin \beta \cos \alpha \sin \alpha_2 - \cos \beta \sin \alpha\right) \\ \theta &= \tan^{-1}\left(\frac{y}{x}\right) = \tan^{-1}\left(\frac{-\sin \beta \cos \alpha_2}{\cos \beta \cos \alpha + \sin \beta \sin \alpha \sin \alpha_2}\right) \end{aligned}\right\} \qquad (37)$$

The limit of integration in equation (36) is obtained by noting that the plane S will be below the far-field point only when $z > 0$. This condition results in

$$\sin \alpha_2 > \frac{\tan \alpha}{\tan \beta}$$

Hence, the contribution to the spectral density of the pressure at the far-field angle β with respect to the jet axis coming from the strip at $x = a$ is given by

$$\mathscr{S}'\left(R, \beta; \omega, \Delta x_1\right) = \int_{\alpha_2{}^*}^{\pi - \alpha_2{}^*} \mathscr{S}\left(r, \theta, \vartheta, \vec{0}; \omega\right) d\alpha_2$$

where r, θ, and ϑ are given by equations (37) and

$$\alpha_2{}^* = \sin^{-1}\left(\frac{\tan \alpha}{\tan \beta}\right)$$

System Calibration

In order to validate the experimental procedures in the measurement of the acoustic intensity, a test was conducted with an experimental point source. The design of the point source was similar to that of the one developed by Atvars, Schubert, Grande, and Ribner (ref. 16). The experiment consisted of evaluating $S_I(0;\omega)$ (eq. (28)) from measurement of the correlation function $S_{\nabla p, \nabla p}(\vec{0}, \xi, \phi; \omega)$ from the experimental point source. This correlation function was measured by using two pressure gradient microphones. The development and calibration of the microphone is presented in appendix B. The result was then compared with the measurement made with a single condenser microphone system placed in the vicinity of the source which determines the intensity directly. The cross spectral density from a point source along $\phi = 45^{\circ}$ at a frequency $f = 1809$ Hz is shown in figure 11, and the extreme end of the spatial correlation extends up to $R_e = 50$ cm.

The intensity becomes

$$S_I(0;\omega) = \frac{4}{2\pi i\omega\rho} \int_0^{R_e} dR_1 \int_0^{\pi/2} d\phi \left[S_{\nabla p, \nabla p}(0, R_1, \phi; \omega) \cos\left(\frac{\omega R_1}{c}\right) iS_{\nabla p, \nabla p}(0, R_1, \phi; \omega) \sin\left(\frac{\omega R_1}{c}\right)\right]$$

The correlation function of $S_{\nabla p, \nabla p}$ as obtained from the curve fitting of figure 12 is represented by

$$S_{\nabla p, \nabla p} = k_5 e^{-k_1 R_1} \cos\left[\frac{\left(k_2^2 \sin \phi + k_3^2 \cos^2 \phi\right)^{1/2}}{k_2 k_3} \left(R_1 + k_4 R_1^2\right)\right]$$

and

$k_1 = 0.051$

$k_2 = 17.0$

$k_3 = 13.20$

$k_4 = 0.053$

$k_5 = 1.890$

The comparison between the results obtained from the integration of the measured correlation with the direct reading of the intensity was within 22 percent, or about 1 dB. This difference is the order of magnitude of the cumulative error to be expected between the two methods used to evaluate the intensity when all possible errors of the two systems of instrumentation which include transducers, auxiliary equipment, correlator, and readout equipment are estimated.

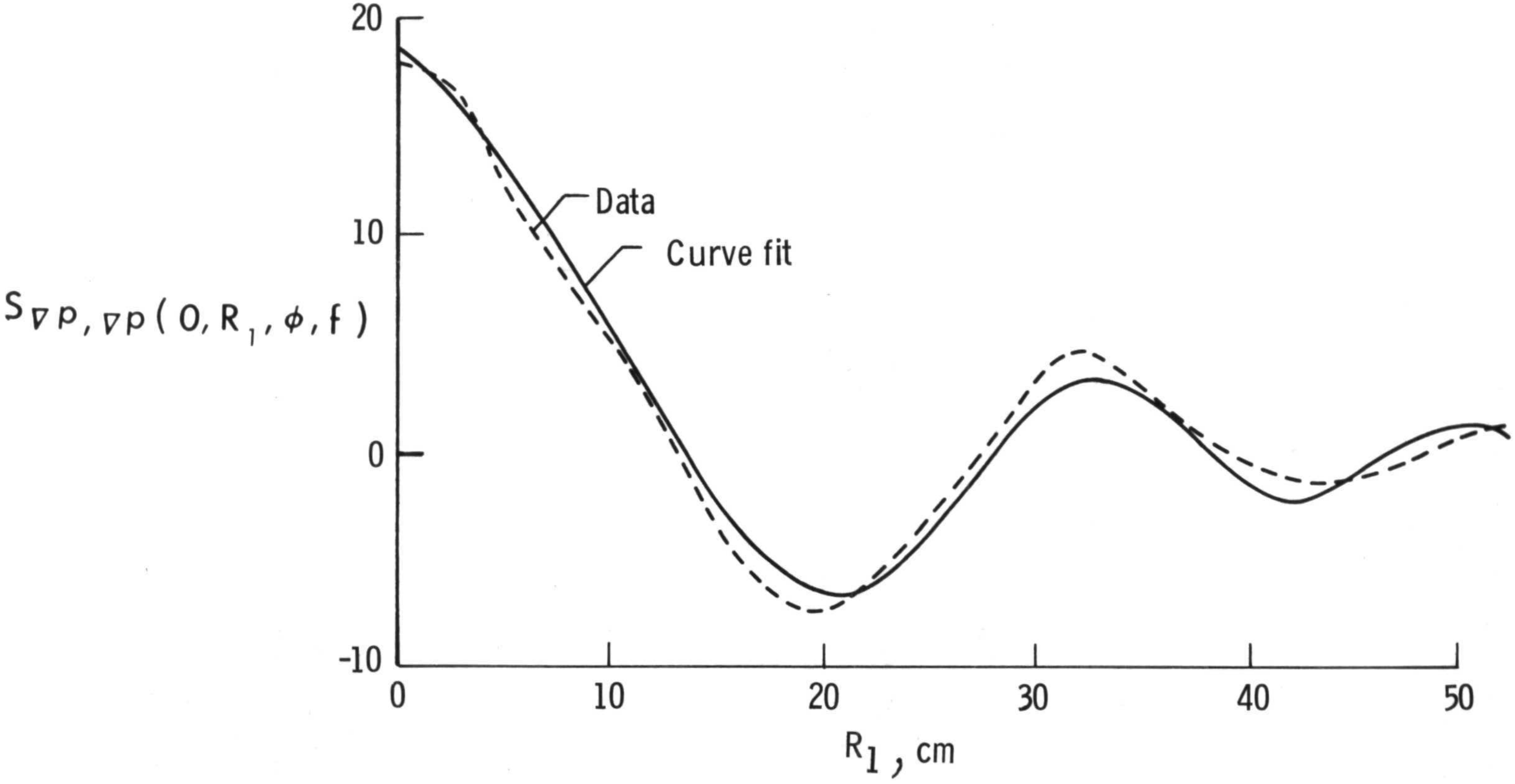

Figure 11.- Cross spectral density for the test case using point source.

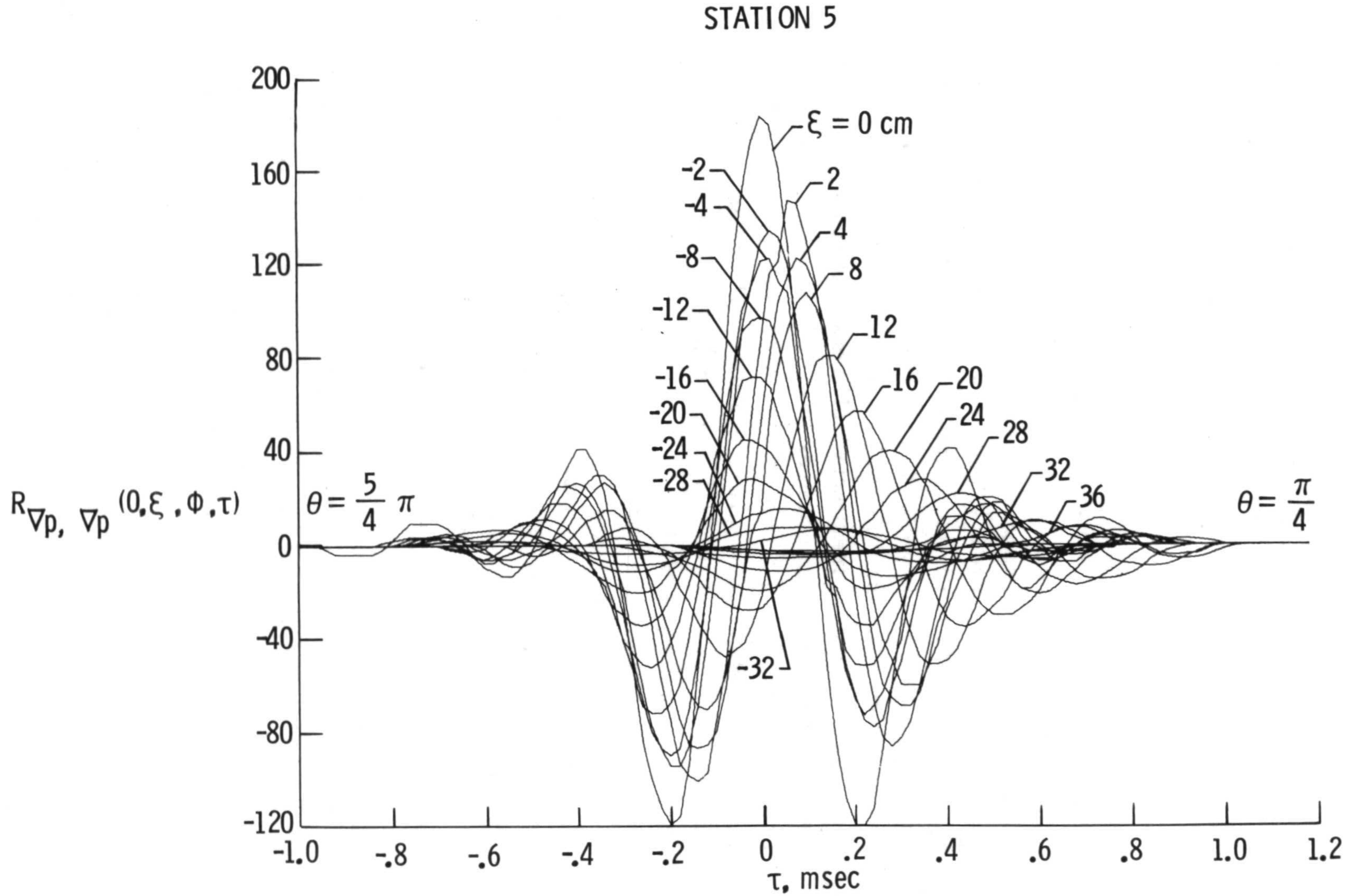

Figure 12.- Broad-band correlation of pressure gradient. $\theta = \pi/4$.

Acoustic Measurements

Correlation measurements were made on a geometrical plane placed at a distance 31.5 cm from the center of the nozzle, at an angle $\alpha = 17^{\circ}20'$ relative to the center line of the jet (fig. 13). The distance from the plane to the jet was chosen from the measurement made of the velocity field so that the pressure on the plane is an acoustic pressure. Measurements of the space-time correlation of the pressure gradient $R_{\nabla p,\nabla p}(0,\xi,\phi;\tau)$ were made within the band between 250 Hz and 3000 Hz at 10 fixed points along the plane at L/D ratios between 0 and 20.56 lying on the projection of the center line of the jet. The correlations were made along three axes lying on the plane and passing through $\vec{r}$. The axis corresponds to the rays of $\phi = 0$ and π; $\pi/4$ and $5\pi/4$; and $\phi = \pi/2$ and $3\pi/2$ in figure 8. Correlation measurements were made for 10 stations along the plane. Typical correlation measurements along these three axes are shown in figures 12, 14, and 15 for station 5 and correspond to $L/D = 9.26$. For higher frequencies, these measurements allowed $R_{\nabla p,\nabla p}(0,\xi,\phi;\tau)$ to be defined with sufficient accuracy whereas for lower frequencies, additional test points on a greater number of axes would be desirable to improve resolution. It is clearly evident that the sound field is nonhomogeneous; this statement implies that as the sound field is radiated away from the jet, it has a preferred downstream direction. The cross correlation is the same along the rays $\phi = 0,\pi$ and $\phi = \pi,0$ because the flow from the jet is also axisymmetric; therefore only the correlation along $\phi = 0$ is shown. The spatial extent of the cross correlation indicates that the unit area of the plane is sensitive to fairly extended regions of the jet especially at large L/D values where the lower frequency predominates the higher. For the stations downstream of station 5, the spatial extent of the correlation $R_{\nabla p,\nabla p}$ along the rays $\theta = \pi/4$ and $\pi/2$ decreases less rapidly with distance than along the rays $\theta = 5\pi/4$ and $3\pi/2$ whereas for stations upstream of station 5, the correlation $R_{\nabla p,\nabla p}$ becomes more homogeneous in space. These results imply that for the stations close to the jet exit, the sound field radiates away from the jet nearly omnidirectionally; whereas for stations further downstream, the sound field is directional. This picture of the correlation field describing the acoustic wave pattern as it emanates from the jet is consistent with the far-field intensity measurements in this experiment and with results of other experiments as described in the literature.

The cross spectral density $S_{\nabla p,\nabla p}(0,\xi,\phi;\omega)$ was obtained by taking the Fourier transform of the broad-band cross correlation for 12 center frequencies between 250 Hz and 3000 Hz at 250-Hz intervals. From the narrow-band correlations, one can construct the wave vector spectrum as was done previously by Maestrello and McDaid (ref. 2). This spectrum displays a pronounced maximum on wave number space which corresponds to the direction of the sound reaching the plane of measurements. Although this spectrum will not be reported, it can be obtained from the available information.

Station	0	1	2	3	4	5	6	7	8	9
L/D	0	945	1.87	3.72	5.54	7.42	9.25	12.98	16.65	20.56

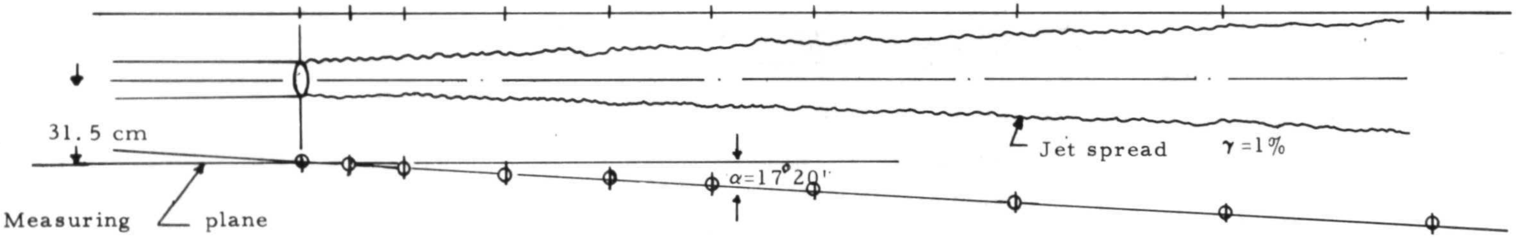

Figure 13.- Geometry of the test setup.

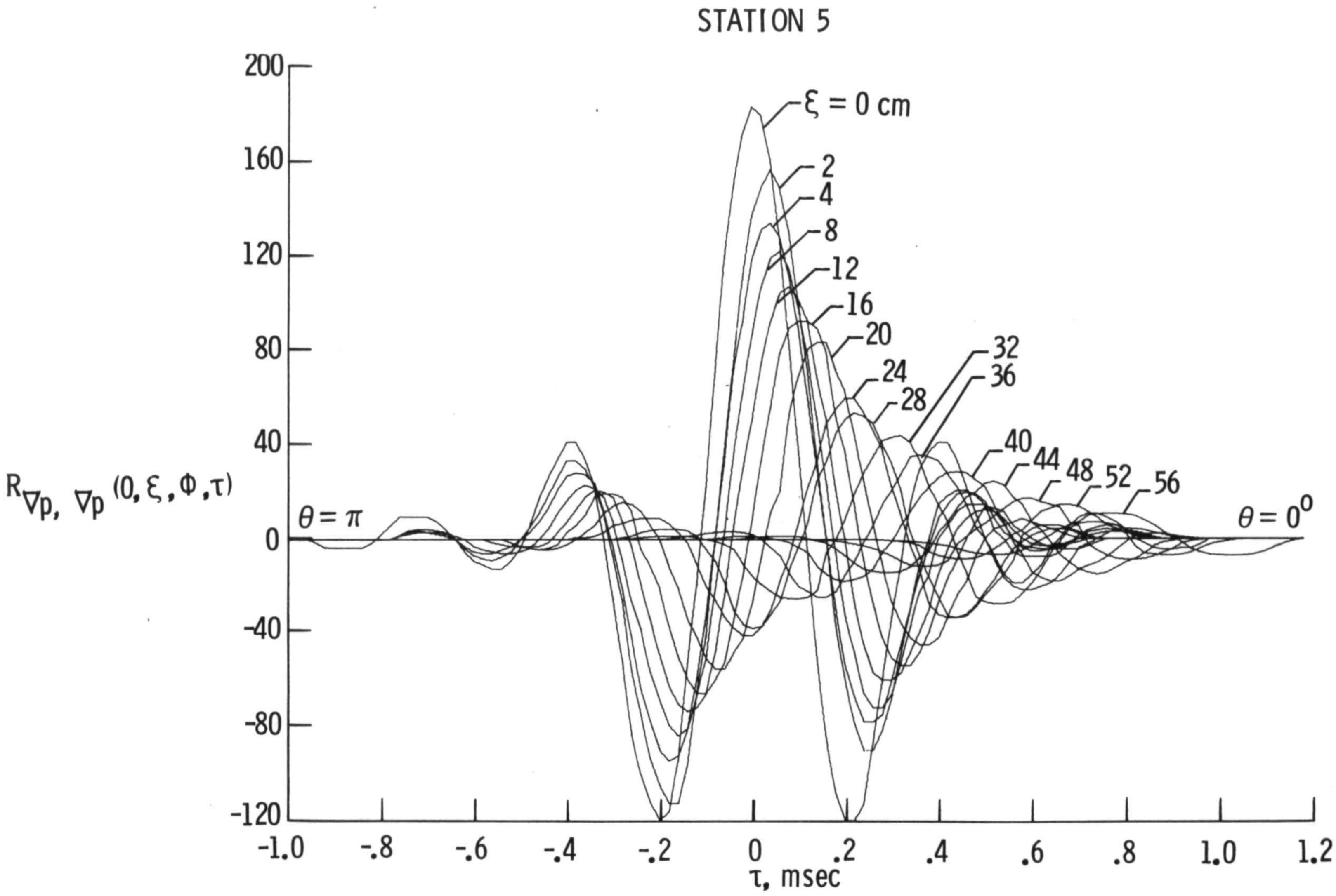

Figure 14.- Broad-band correlation of pressure gradient. $\theta = 0^\circ$.

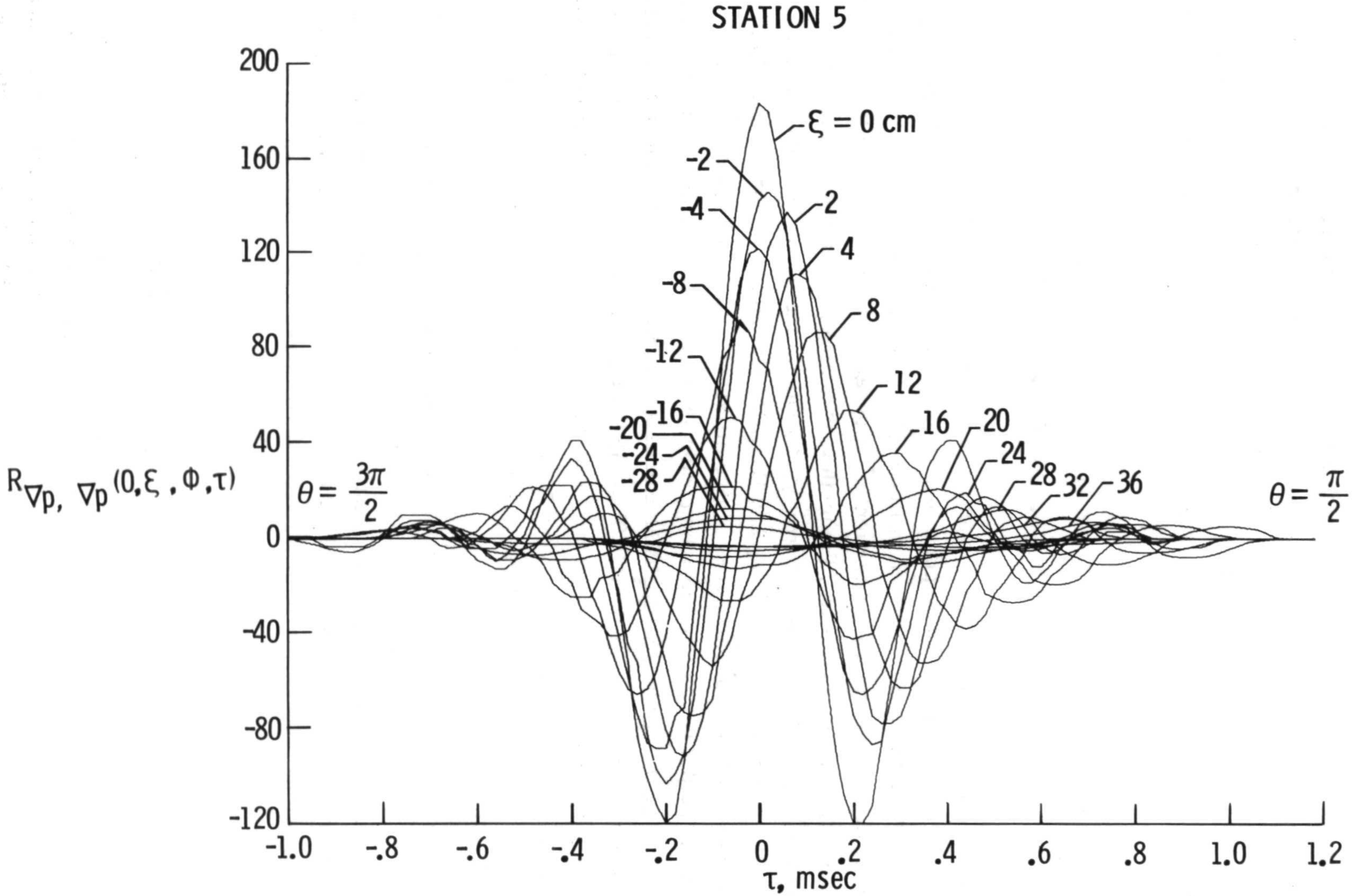

Figure 15.- Broad-band correlation of pressure gradient. $\theta = \pi/2$.

An additional measurement of the pressure field was made at one fixed location along the jet by using two condenser pressure microphones to insure that the choice made on the position of the plane along the jet is consistent with the measurement made of the velocity field. This measurement shows that the velocity along the plane satisfies the acoustic wave equation. The result shows that all the convected components except that for the frequency 250 Hz of the cross correlation about the geometrical plane are acoustic components.

PHOTOGRAPHIC REPRESENTATION OF SOUND FIELD PATTERN EMANATING FROM A JET

Noise radiation from jet exhausts can be represented by a pattern of colors, obtained by means of a photographic plate, each color corresponding to a different intensity level of noise. This effect is seen in figure 16 which represents the noise field from a jet in that region where the wave equation is reasonably well satisfied. Although this is a new application in aeroacoustics, the method is analogous to a color image formed in a television picture tube. This photographic technique was first developed by Kock and Harvey (ref. 17) and by J. T. Rainey and D. G. Neville (ref. 18). The colors in the picture are the result of time exposures of five different color light bulbs, each bulb being triggered by the output voltage of a nearby condenser microphone mounted on a swinging arm. The microphone traverses successive arcs arranged in such a manner that their loci are a vertical plane at an angle 17°20' to the thrust axis and at a distance of 31.5 cm from a 6.25-cm-diameter nozzle. The resulting figure 16 is made up of superimposed elliptically shaded color patterns stretched along the flow axis. The maximum intensity region is represented by red; and orange, green, and yellow represent successive 2-dB decrements in noise level.

This technique should be developed further because the display of the sound field patterns is a useful representation of the distribution of the sound pressure level. This technique can easily be extended to represent sound energy, energy density flux as well as propagation path, and all quantities required to evaluate the mechanism of sound generation and propagation.

RESULTS AND DISCUSSION

Evaluation of the Acoustic Energy Density Flux

In order to insure the accuracy of the techniques employed in this analysis, comparison is made in this discussion between the total acoustic power and the acoustic intensity, evaluated by equations (28) and (36), respectively, with the corresponding quantities directly measured by a simple microphone in the far field. New information of

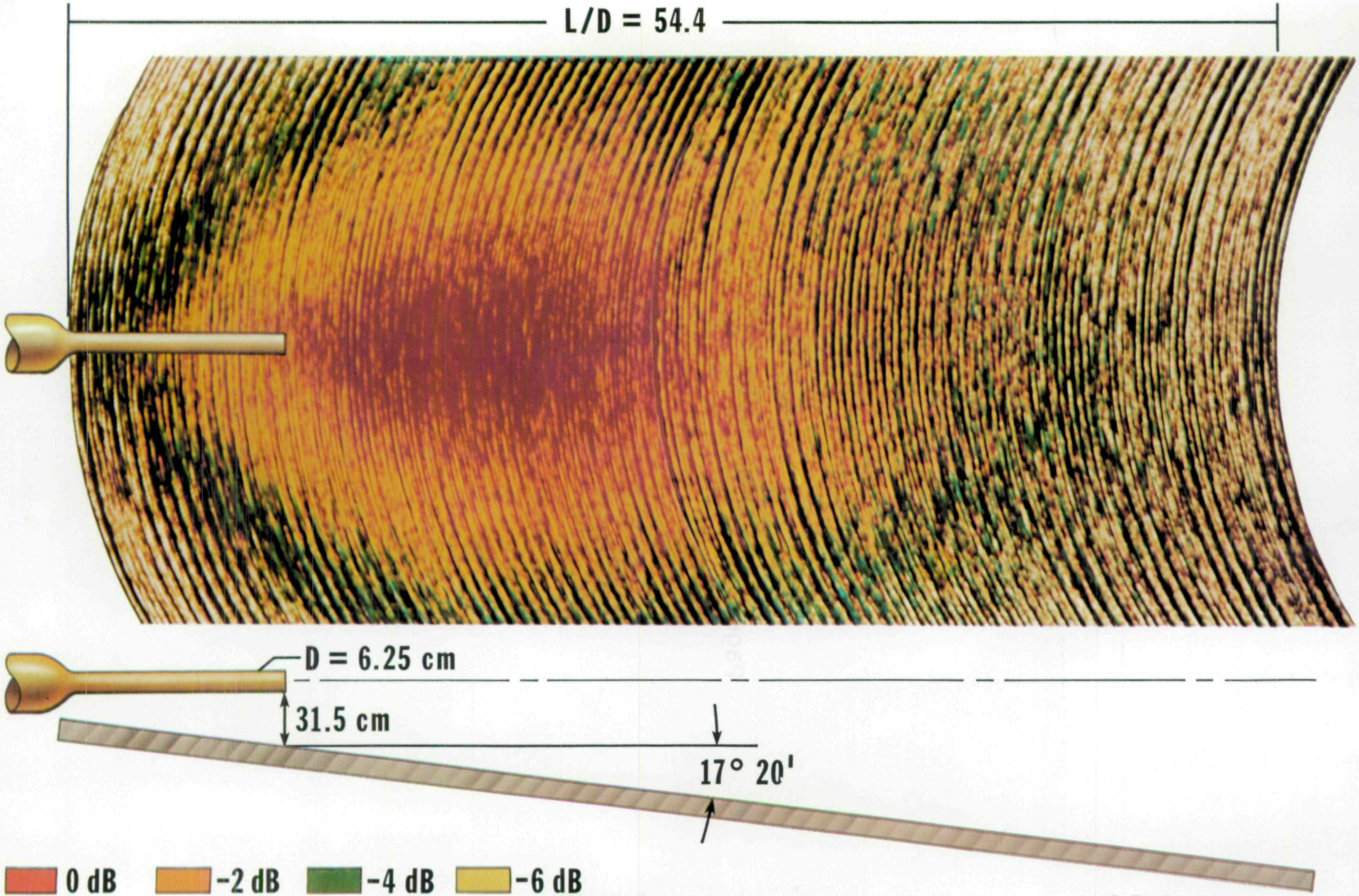

L-73-3072

Figure 16.- Broad-band jet noise field visualization. U_j = 213 m/sec; lens width, 166 cm.

Page Intentionally Left Blank

acceptable accuracy about noise emanating from a jet is presented, namely, the distribution of acoustic power along the plane of measurements and the far-field intensity resulting from the contribution of sound emanated from the various stations along the plane.

Evaluation of the acoustic energy density flux $S_I(0,f)$ (eq. (28)) is shown in figure 17, for 10 stations along the plane. The flux is normalized with the mean value $\int_0^\infty S_I(0,f)\,df$ at each station and is plotted in terms of the Strouhal number fD/U_j and in terms of L/D, where D is the jet diameter, U_j is the jet exit velocity, and L is the distance from nozzle exit to the projection of the plane into the jet axis. (See fig. 13.) It is evident that the higher frequency components are contributed mostly from the region near the jet exit and this contribution diminishes rapidly with increasing distance downstream, whereas lower frequency components, mainly 750 Hz and 1000 Hz (corresponding to $fD/U_j = 0.225$ and 0.3), are contributed more evenly from all stations along the plane. These lower frequencies also correspond to the peak amplitude power spectral density in the far field.

Some caution must be exercised in interpreting the source distribution from the evaluation of the acoustic energy flux. The distribution of the acoustic energy density flux on the plane near the jet cannot be interpreted as an equivalent source distribution. What is evaluated on the plane is relevant only to the sound field as it emanates from the outer boundary of the jet and not in the manner in which the source originates sound since the source inside the jet has finite life time, and the distribution of the radiation depends on the resultant instantaneous strength by the superposition of number of multipole fields. As the pressure is released from the source, it interacts with the jet stream extracting energy therefrom as well as imparting energy thereto. The full convected wave equation provides the necessary clue as to how the pressure is transmitted through the flow. The sources in the jet appear and disappear as they move imbedded in the moving stream and indicate that in this mechanism, the steady-state condition does not exist. This is one of the main reasons why the sound field is evaluated outside the jet before it is evaluated from the inside.

The broad-band emission of sound per unit length of the jet evaluated on the plane is shown in figure 18. It is obtained by rotating the plane around the jet and adding the contribution made per unit area of the plane. Since the jet is axisymmetric, it is assumed that the power per unit area of the plane is the same at the same radial position of the plane with respect to the jet. The sound emitted peaks at approximately 9 jet diameters downstream of the jet and it varies in amplitude by a factor of better than two at the extreme stations. Intuitively, one would expect the distribution of sources inside the jet to have a distribution which is shifted more closely to the jet exit than the one measured on the plane due to convection and refraction as the sound crosses the flow on its way out of the jet.

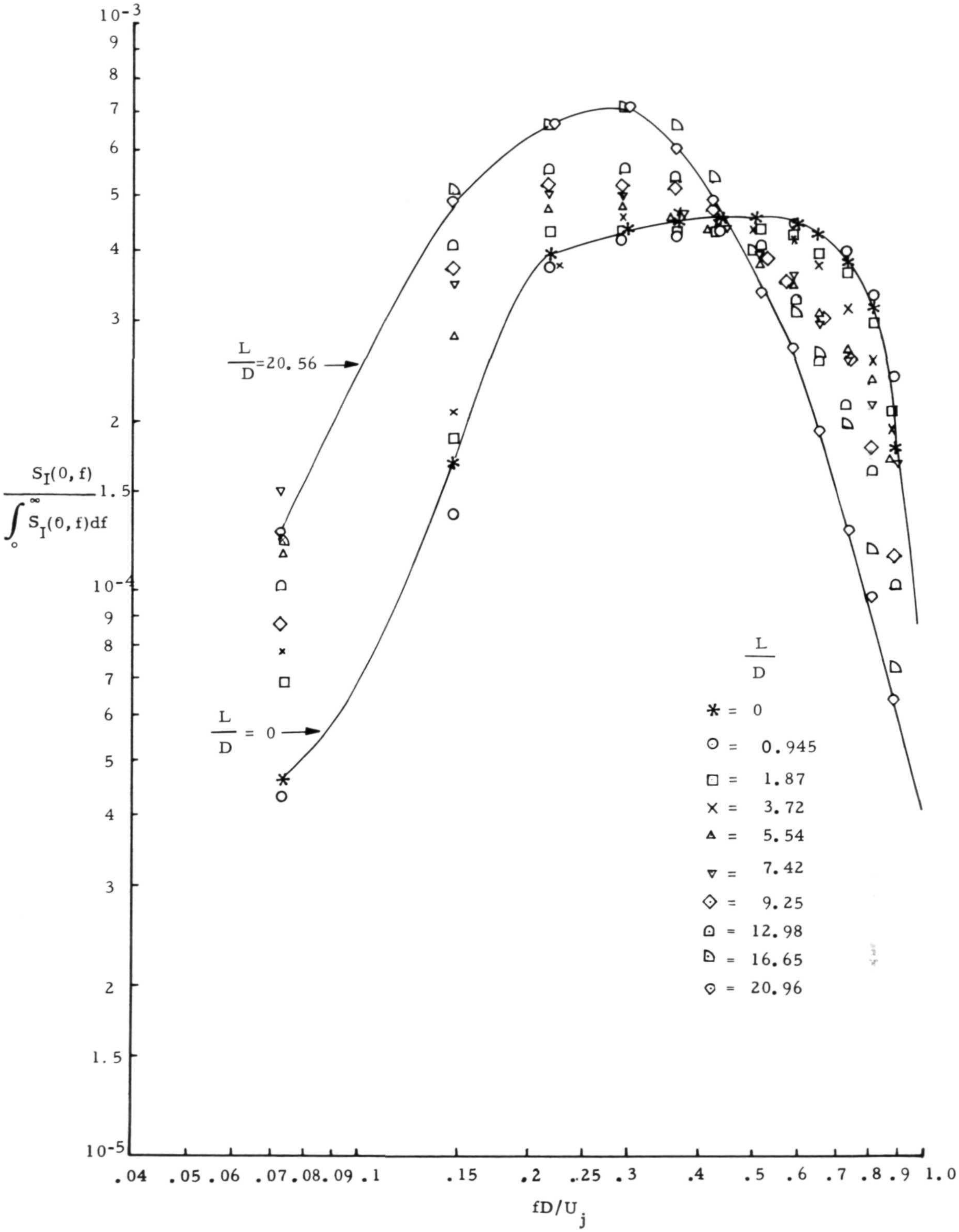

Figure 17.- Normalized acoustic power per unit area of the plane between stations 0 and 9.

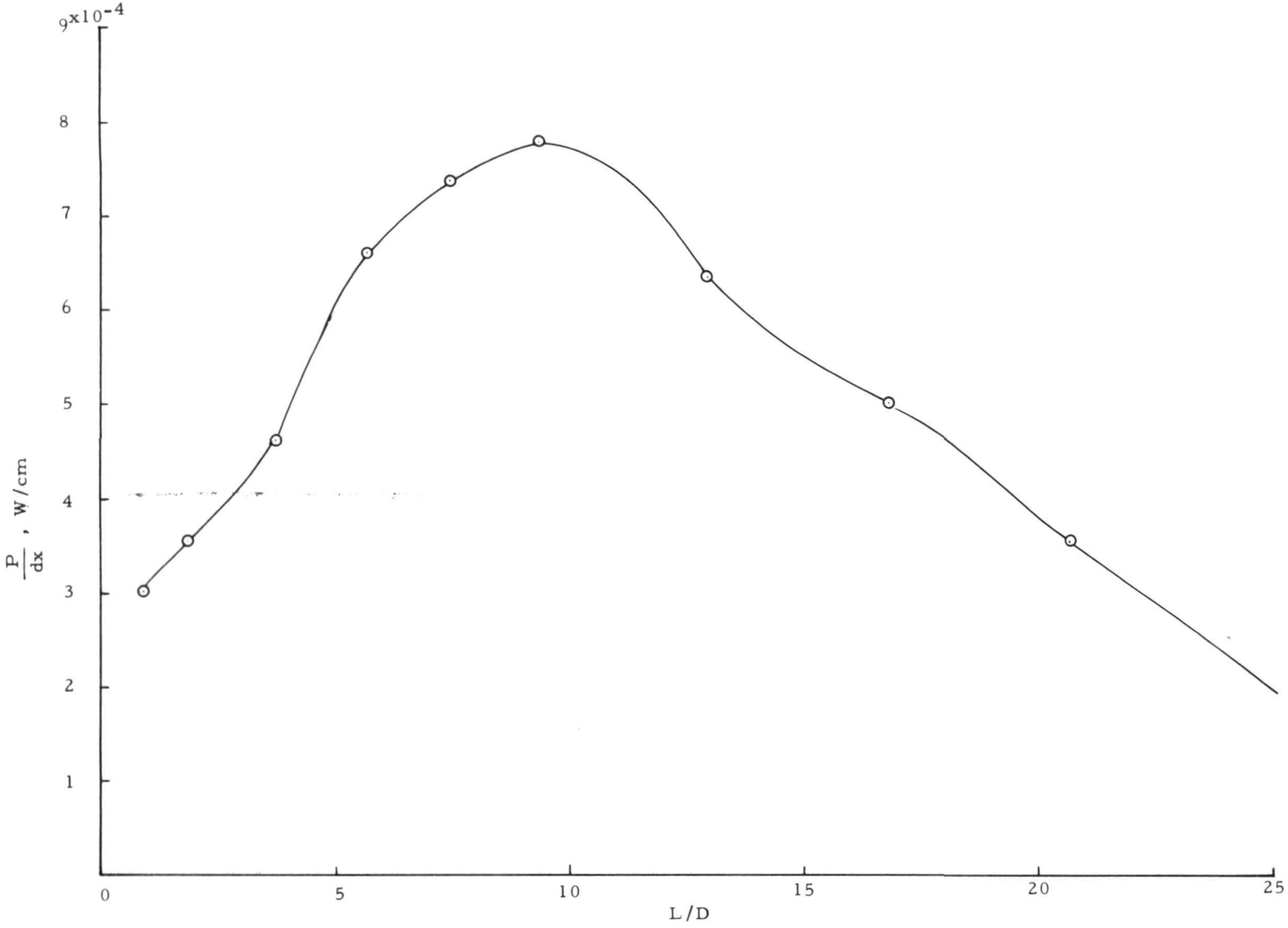

Figure 18.- Variations of acoustic power emission from a unit lens along the plane.

In order to insure that the area inside the curve of figure 18 corresponds to the correct value of the total acoustic power, comparison was made with far-field total power measurements between 250 Hz and 3000 Hz. The direct far-field measurement was obtained by integrating elemental areas around a 3.65-meter-diameter sphere. The results show that the total acoustic power from far-field measurements is 0.82 watt and the total acoustic power from figure 18 is 0.74 watt.

The comparison is remarkably close about 0.5 dB between the two approaches; it validates, at least in part, that this technique is of practical significance in obtaining the distribution of the acoustic power along the jet. Additional information on the distribution of the acoustic power along the jet can be obtained by plotting the power per unit length (normalized with the total jet power) against Strouhal number fD/U_j (fig. 19). Peak amplitudes occur for $fD/U_j = 0.3$ and 0.225 which also is the range of Strouhal numbers where the far-field power spectral density peaks. The variation of the power with distance is very gradual except for the initial few diameters. For much higher Strouhal numbers the distribution shifts close to the jet exit and the field is not as broadly spaced as that for low Strouhal numbers. Therefore, the significant medium frequency far-field contribution comes from a region of the jet conical outer boundary where the emission of sound is stretched well beyond 10 nozzle diameters and is not as localized as those for the higher Strouhal number components. However, as none of the components show strong localized regions of sound emanating from a particular part of the jet, this result tends to suggest that there are no highly localized directional sources in the flow. These results relate the distribution of sound emission on the plane and ought not to be compared with the distribution of sources obtained by using similarity considerations by Ribner (ref. 19), Powell (ref. 20), Lilley (ref. 21), nor with recent measurements of direct correlation made by Lee and Ribner (ref. 9) since one refers to the source inside the jet, whereas this work refers to the distribution of sound as it exited from the jet.

Evaluation of Far-Field Intensity

Evaluation of far-field intensity $\mathcal{I}'(R,\beta;\omega,\Delta x)$ (eq. (36)) was checked out by using a known function for $S_{\nabla p,\nabla p}(\vec{0},\xi,\phi;\omega)$ with omnidirectional spatial distribution over the axis of the plane. The far-field intensity $\mathcal{I}'$ shows an equivalent omnidirectional intensity except in the region where the angle β approaches the angle of the plane α for reasons presented in the formulation of the problem. This comparison validates the numerical procedure used in evaluating $\mathcal{I}'$. Computation of the function $\mathcal{I}'$ was made at two far-field angles, 90° and 45°, and the results are plotted in terms of the Strouhal number fD/U_j in figures 20 and 21. In addition, the far-field intensity obtained by adding the contributions to the intensity evaluated along each station up to $L/D = 20.96$ was

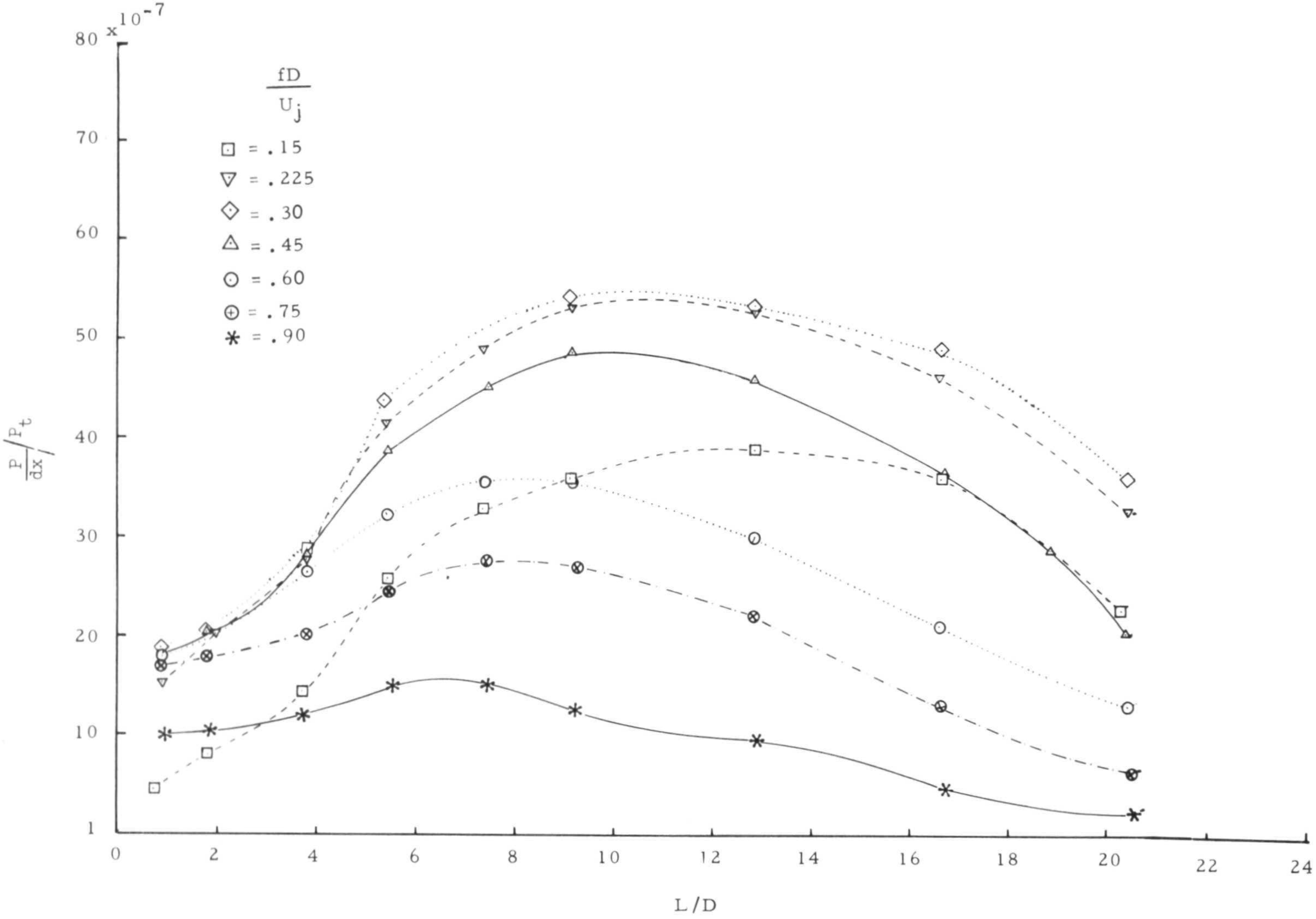

Figure 19.- Variations of the acoustic power along the plane at various fD/U_j.

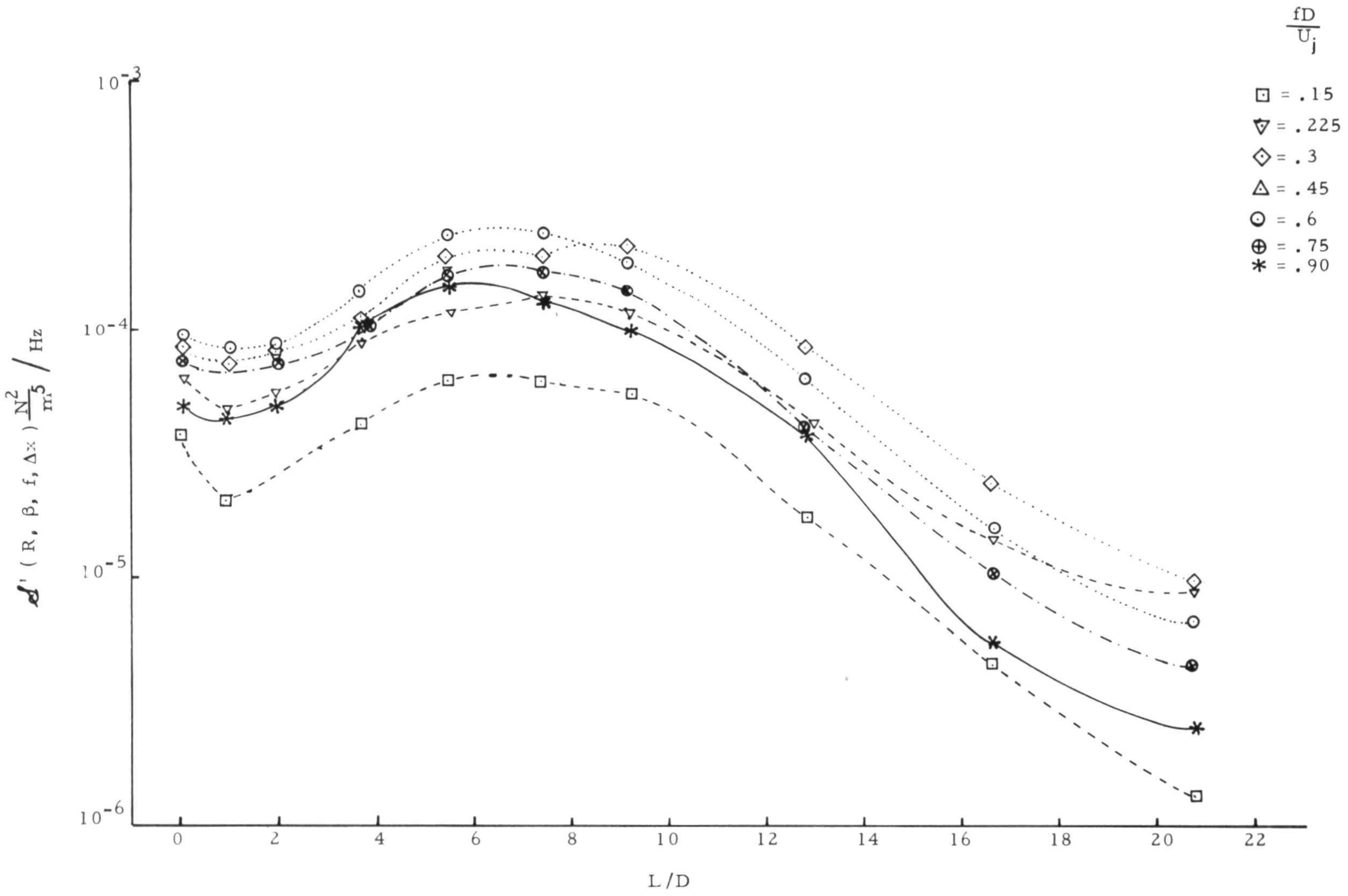

Figure 20.- Contribution to far-field intensity at $\beta = 90^\circ$, R = 3.65 meters along the plane computed from equation (36) for different locations.

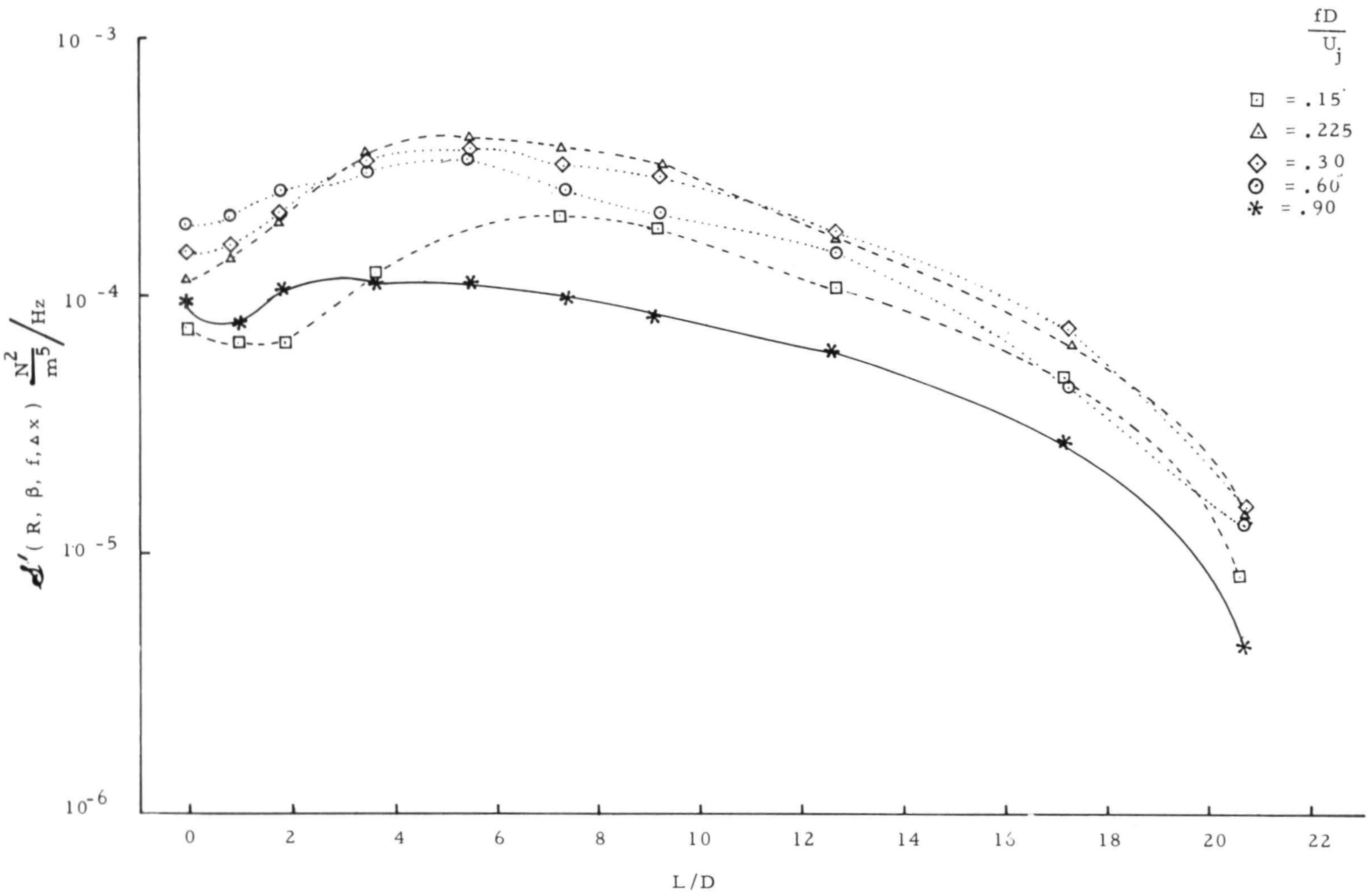

Figure 21.- Contribution to far-field intensity at $\beta = 45^{\circ}$, R = 3.65 meters along the plane computed from equation (36) from different locations.

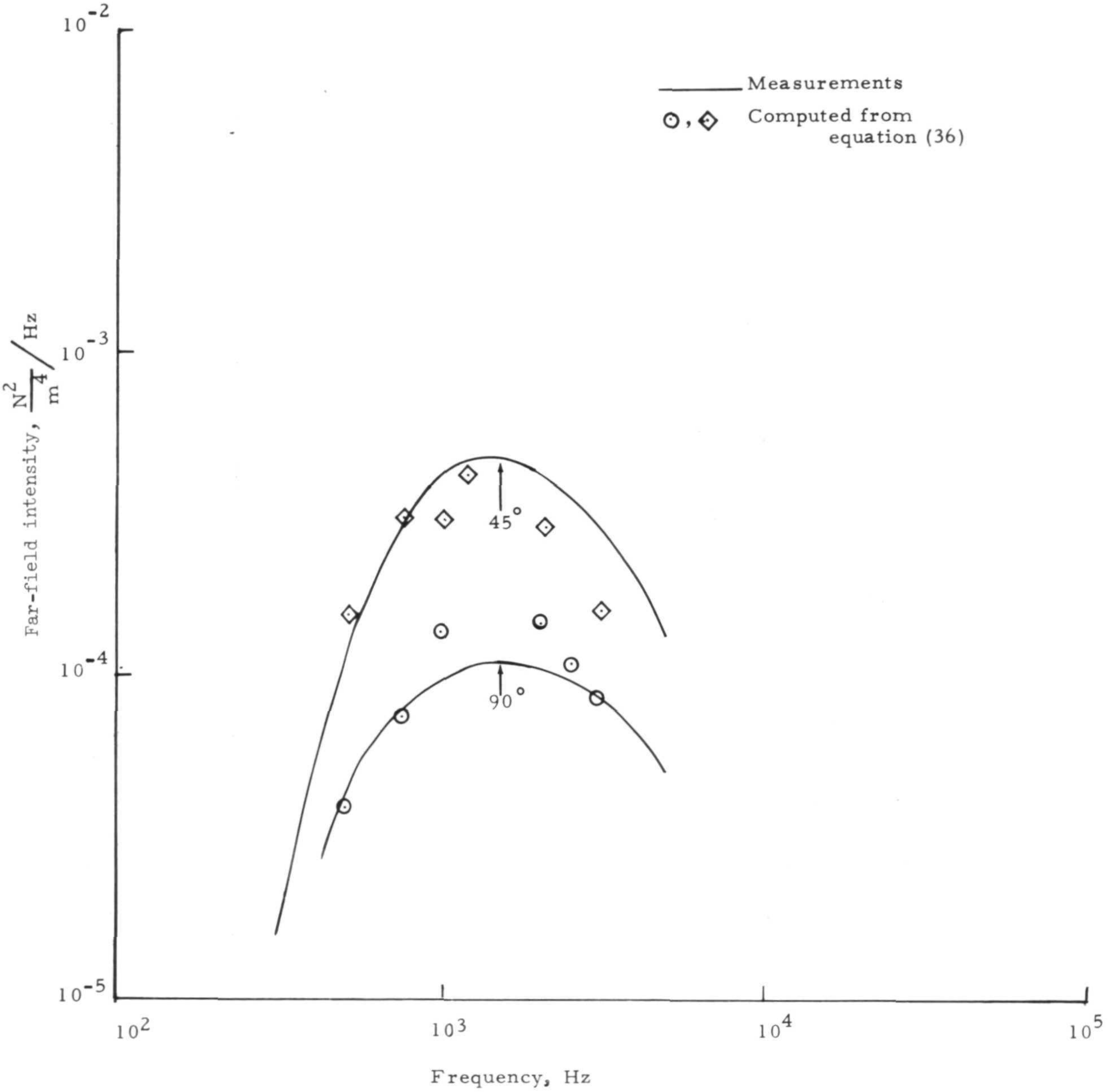

Figure 22.- Far-field intensity for $\beta = 45^\circ$ and 90°.

compared with a single microphone measurement in the far field (fig. 22). The agreement for both 90° and 45° is satisfactory.

The additional contribution by intensity in the region of the jet beyond $L/D = 20.96$ is not significant, as deduced from figures 20 and 21. In this experiment the minimum acceptable far-field angle β is approximately 30° and is limited by the plane angle α. One can reduce the plane angle, however, by increasing the distance between the plane and the axis of the jet. (See fig. 13.)

The distribution $\mathscr{I}'$ is the far-field intensity as made up of contributions from each station on the plane plotted in terms of the projection of the plane into the jet axis L/D. Conclusions can be drawn from figures 20 and 21 regarding what is the most significant region of the jet contributing to the far field for a given Strouhal number. It is significant from the figures that $fD/U_j = 0.30$ and 0.60 contributed mostly at $\beta = 90^\circ$, whereas at $\beta = 45^\circ$ most contribution comes from $fD/U_j = 0.30$, 0.225, and 0.60, and indicates an apparent shift in predominant spectral distributions to the lower frequencies between 90° and 45°.

The distribution $\mathscr{I}'$ for $\beta = 90^\circ$ has a more clearly defined maximum value as L/D varies than that for $\beta = 45^\circ$ which shows a more extended contribution along the various stations on the plane. The intensity amplitude between the two far-field angles varies in a systematic manner, decreasing between 90° and 45°. The directivity and the intensity at each station along the plane is dependent on the cross correlation of the pressure on the plane, and since the plane is relatively close to the jet boundary, these results provide an initial clue of the contribution of each station of the jet to some particular far-field angle. This result shows that the emissions of sound from various stations differ more with far-field angle than with Strouhal number, as far as the spatial extent of emission at various stations is concerned; the Strouhal number only adjusts the relative amplitude of emission. This result may clarify some directivity anomalies reported by Lush (ref. 22). Another interesting observation is that there appears to be some significant shifting of the peak of the distribution with far-field angle and with Strouhal number; this trend, however, is not well characterized. It could be due to some inaccuracy of the data between adjacent stations; any inaccuracy, however, is not expected to alter drastically the observed behavior. This last observation may be more apparent since the change in far-field angle tends to compress or stretch the contribution made by each station to the far-field point.

CONCLUDING REMARKS

This paper establishes the relationship of sound emanating from various regions of a well-defined conical outer boundary of a subsonic jet with the far-field directivity and intensity distribution. The technique used permits acoustic measurements to be taken close to the regions from which the sound emanates without getting involved in detailed measurements of the flow field inside the jet.

To define the geometrical plane where acoustic measurements were carried out and which, in turn, define the conical outer boundary, velocities were obtained by mapping of the flow field about the jet outside the vortical flow. This mapping shows two distinct regions of interest: the region close to the interface, where Laplace's equation is valid, and the mean-square value of the velocity decreases inversely to the fourth power of distance, as originally predicted by Phillips, and a region further from the jet, where the acoustic wave equation is satisfied with the mean-square velocity decreasing inversely to the second power of the distance. The induced flow approaches the jet at approximately 90° from the flow axis and the mean radial velocity component decreases inversely with the first power of the distance. These results are consistent with the prediction made by Stewart.

The results show that the broad-band acoustic power evaluated on the geometrical plane peaks at approximately 9 diameters downstream from the nozzle. Also, the narrow-band acoustic power at a Strouhal number of about 0.3 predominates over nearly the entire length of the jet. The contribution of the sound from the plane of measurements to the far field, however, depends less on the Strouhal number than on the field angle. This result may clarify some directivity anomalies reported by Lush.

One can observe that the far-field intensity distributions along the jet differ significantly for the angles of 45° to 90°. At 45° the intensity distribution for Strouhal number 0.9 is far below the mean level of intensity for Strouhal number of about 0.3, whereas at 90° for the Strouhal number at 0.9, the intensity distribution is much closer to the peak distribution.

These measurements show that the far-field frequency spectrum peak is related to the spatial extent of the region where the sound emanates from the jet. The 45° components emanate from an extended region of the jet, over 17 diameters long, whereas the 90° components of the sound field are concentrated in a narrower region. It is apparent that a large increase in jet velocity cannot significantly alter the spatial extent of the region from which the sound emanates at 45° unless the flow becomes supersonic. The change will affect the amplitude distribution but will not shift the peak frequency since the amplitude of the higher frequency components cannot change enough relative to that at a Strouhal number of about 0.3 to alter the peak. However, for the 90° components, the higher velocity can easily alter the peak frequency since the contributions from the different Strouhal numbers are relatively close together. Thus, it may again be inferred from the present investigation that the far-field spectrum peak depends more on the far-field angle than on the Strouhal number for far-field angles of the order of 45° or less. The Strouhal number dependence of the normalized spectrum distribution becomes significant only for large far-field angles.

These results can also provide information relevant to sound suppression by means of surface shielding or shielding by refraction, obtained by tailoring the temperature gradient of a jet, in terms of the length of the surface or that of the refraction zone. This conclusion is drawn from the spatial extent of the region where the sound is emanated from the jet. At the 45° far-field angle, substantial suppression can only be achieved when the shielding surface or the refractive zone extends beyond 20 nozzle diameters downstream and beyond 10 nozzle diameters laterally as seen from the lateral cross correlation whereas for 90° far-field angle suppression can be achieved by using a smaller surface.

Langley Research Center,
National Aeronautics and Space Administration,
Hampton, Va., May 23, 1973.

APPENDIX A

NUMERICAL CALIBRATION FOR THE ACOUSTIC ENERGY FLUX

To check the general analysis equation (eq. (28)), consider a point source of strength f(t) located directly below the plane S as shown in figure 8, at 0,0,r,h. The pressure at any point $\vec{r}$ is given by

$$p(\vec{r},t) = \frac{f\left(t - \frac{R}{c}\right)}{R} \tag{A1}$$

where

$$R = \left[x^2 + y^2 + (z + h)^2\right]^{1/2} = \left[\xi^2 + (z + h)^2\right]^{1/2}$$

The pressure gradient normal to S at any point $\vec{r}_o$ on the plane $z = 0$ is thus

$$\frac{\partial p(\vec{r}_o,t)}{\partial z} = -\frac{h}{R_o{}^3}\left[\frac{R_o}{c} f'\left(t - \frac{R_o}{c}\right) + f\left(t - \frac{R_o}{c}\right)\right] \tag{A2}$$

where

$$R_o = \left(\xi^2 + h^2\right)^{1/2}$$

The correlation of the pressure gradient about the origin is

$$\begin{aligned}
R_{\nabla p, \nabla p}\left(\vec{0}, \xi, \phi; \tau\right) &= \left\langle \frac{\partial p\left(\vec{0}, t+\tau\right)}{\partial z} \frac{\partial p^*\left(\vec{r}_o,t\right)}{\partial z} \right\rangle \\
&= \left\langle \frac{h^2}{h^3 R_o{}^3}\left[\frac{h}{c} f'\left(t + \tau - \frac{h}{c}\right) + f\left(t + \tau - \frac{h}{c}\right)\right]\left[\frac{R_o}{c}(f')^*\left(t - \frac{R_o}{c}\right) + f^*\left(t - \frac{R_o}{c}\right)\right]\right\rangle \\
&= \frac{1}{hR_o{}^3}\left[\frac{hR_o}{c^2}\left\langle f'\left(t + \tau - \frac{h}{c}\right)(f')^*\left(t - \frac{R_o}{c}\right)\right\rangle + \frac{h}{c}\left\langle f'\left(t + \tau - \frac{h}{c}\right) f^*\left(t - \frac{R_o}{c}\right)\right\rangle\right. \\
&\quad \left. + \frac{R_o}{c}\left\langle f\left(t + \tau - \frac{h}{c}\right)(f')^*\left(t - \frac{R_o}{c}\right)\right\rangle + \left\langle f\left(t + \tau - \frac{h}{c}\right)(f')^*\left(t - \frac{R_o}{c}\right)\right\rangle\right]
\end{aligned} \tag{A3}$$

By introducing the variables

$$t_1 = t - \frac{R_o}{c}$$

$$t_2 = \tau + \frac{R_o}{c} - \frac{h}{c}$$

$$R_{\nabla p, \nabla p}\left(\vec{0}, \xi, \phi; t_2\right) = \frac{1}{hR_o^{\,2}}\left[\frac{hR_o}{c^2}\left\langle f'\left(t_1 + t_2\right)(f')^*\left(t_1\right)\right\rangle + \frac{h}{c}\left\langle f'\left(t_1 + t_2\right)f^*\left(t_1\right)\right\rangle \right.$$
$$\left. + \frac{R_o}{c}\left\langle f\left(t_1 + t_2\right)(f')^*\left(t_1\right)\right\rangle + \left\langle f\left(t_1 + t_2\right)f^*\left(t_1\right)\right\rangle\right] \qquad \text{(A4)}$$

and noting that

$$R_{ff}\left(t_2\right) = \left\langle f\left(t_1 + t_2\right)f^*\left(t_1\right)\right\rangle$$

$$\frac{\partial}{\partial t^2} R_{ff}\left(t_2\right) = \left\langle f'\left(t_1 + t_2\right)f^*\left(t_1\right)\right\rangle = -\left\langle f\left(t_1 + t_2\right)(f')^*\left(t_1\right)\right\rangle$$

$$\frac{\partial^2}{\partial t^2} R_{ff}\left(t_2\right) = -\left\langle f'\left(t_1 + t_2\right)(f')^*\left(t_1\right)\right\rangle$$

one obtains

$$R_{\nabla p, \nabla p}\left(\vec{0}, \xi, \phi; t_2\right) = \frac{1}{hR_o^{\,3}}\left[-\frac{hR_o}{c^2}\frac{\partial^2 R_{ff}\left(t_2\right)}{\partial t_2^{\,2}} + \frac{h}{c}\frac{\partial R_{ff}\left(t_2\right)}{\partial t_2} - \frac{R_o}{c}\frac{\partial R_{ff}\left(t_2\right)}{\partial t_2} + R_{ff}\left(t_2\right)\right] \qquad \text{(A5)}$$

By taking the Fourier transform,

$$\begin{aligned} S_{\nabla p, \nabla p}\left(\vec{0}, \xi, \phi; \omega\right) &= \int_{-\infty}^{\infty} e^{-i\omega\tau} R_{\nabla p, \nabla p}\left(\vec{0}, \xi, \phi; \tau\right) d\tau \\ &= \int_{-\infty}^{\infty} e^{-i\omega\left(t_2 - \frac{R_o}{c} + \frac{h}{c}\right)} R_{\nabla p, \nabla p}\left(\vec{0}, \xi, \phi, t_2\right)t_2 \\ &= e^{i\omega\left(\frac{R_o}{c} - \frac{h}{c}\right)} \frac{1}{hR_o^{\,3}}\left[\omega^2 \frac{hR_o}{c^2} + i\omega\left(\frac{h}{c} - \frac{R_o}{c}\right) + 1\right] S_{ff}(\omega) \\ &= \frac{S_{ff}(\omega)}{R_o^{\,2}}\left[\frac{\left(1 + i\frac{\omega}{c}h\right)e^{i\frac{\omega}{c}h}}{h}\right]\left[\frac{\left(1 - i\frac{\omega}{c}R_o\right)e^{i\frac{\omega}{c}R_o}}{R_o}\right] \end{aligned} \qquad \text{(A6)}$$

where

$$S_{ff}(\omega) = \int_{-\infty}^{\infty} d\tau \, e^{-i\omega\tau} \, R_{ff}(\tau) \tag{A7}$$

Hence, from equation (28),

$$\begin{aligned}
S_I(\vec{0};\omega) &= \frac{1}{2\pi i\omega\rho} \int_0^{2\pi} d\phi \int_0^{\infty} d\xi \, e^{i\frac{\omega}{c}\xi} \, S_{\nabla p,\nabla p}(\vec{0},\xi,\phi;\omega) \\
&= \frac{1}{i\omega\rho} \int_0^{\infty} d\xi \, e^{i\frac{\omega}{c}\xi} \, \frac{S_{ff}(\omega)}{\left(\xi^2 + h^2\right)} \left[\frac{\left(1 + i\frac{\omega}{c}h\right)e^{-i\frac{\omega}{c}h}}{h}\right] \left\{\frac{\left[1 - i\frac{\omega}{c}\left(\xi^2 + h^2\right)^{1/2}\right] e^{i\frac{\omega}{c}\left(\xi^2+h^2\right)^{1/2}}}{\left(\xi^2 + h^2\right)^{1/2}}\right\} \\
&= \frac{\left(1 + i\frac{\omega}{c}h\right)e^{-i\frac{\omega}{c}h} \, S_{ff}(\omega)}{i\omega\rho h} \int_0^{\infty} d\xi \, \frac{\left[1 - i\frac{\omega}{c}\left(\xi^2+h^2\right)^{1/2}\right] e^{i\frac{\omega}{c}\left[\left(\xi^2+h^2\right)^{1/2}+\xi\right]}}{\left(\xi^2 + h^2\right)^{3/2}}
\end{aligned} \tag{A8}$$

The exact answer for the intensity is found by considering

$$I(\vec{0};\tau) = \left\langle p(\vec{0}, t+\tau) V_z^{*}(\vec{0},t) \right\rangle$$

Thus, differentiation of this expression gives

$$\begin{aligned}
\frac{\partial I(\vec{0};\tau)}{\partial\tau} &= -\left\langle p(\vec{0}, t+\tau) \frac{\partial V_z^{*}(\vec{0},t)}{\partial t} \right\rangle \\
&= \frac{1}{\rho} \left\langle p(\vec{0}, t+\tau) \frac{\partial p(\vec{0},t)}{\partial z} \right\rangle
\end{aligned}$$

Substituting the pressure and gradient from equations (A1) and (A2)

$$\begin{aligned}
\frac{\partial I(\vec{0};\tau)}{\partial\tau} &= -\frac{1}{\rho ch^2} \left\langle f(t_1 + \tau)(f')^{*}(t_1) \right\rangle - \frac{1}{\rho h^3} \left\langle f(t_1 + \tau) f^{*}(t_1) \right\rangle \\
&= \frac{1}{\rho ch^2} \frac{\partial R_{ff}(\tau)}{\partial\tau} - \frac{1}{\rho h^3} R_{ff}(\tau)
\end{aligned}$$

where

$$t_1 = t - \frac{h}{c}$$

The Fourier transform of the intensity is

$$\begin{aligned} S_I(\vec{0};\omega) &= \int_{-\infty}^{\infty} I(\vec{0};\tau)\, e^{-i\omega\tau}\, d\tau \\ &= \frac{1}{i\omega} \int_{-\infty}^{\infty} \frac{\partial I(\vec{0};\tau)}{\partial \tau}\, e^{-i\omega\tau}\, d\tau \\ &= \left(1 + i\frac{c}{\omega h}\right) \frac{S_{ff}(\omega)}{\rho c h^2} \end{aligned} \tag{A9}$$

This equation should be equal to equation (A8).

APPENDIX B

DEVELOPMENT AND CALIBRATION OF THE PRESSURE GRADIENT TRANSDUCER

The evaluation of the integrand $S_{\nabla p, \nabla p}(\vec{0}, \xi, \phi, \omega)$ is made from measurements of the correlations of the pressure gradient in a plane near the boundary of the jet. The selection of a pressure gradient transducer over other types of pressure transducers was made because of its directional characteristic, its discrimination against distant sound sources, and its rejection of randomly incident background noise. The pressure gradient transducer, shown in figure 23, is of the capacitance type, an "electret" foil being used. It is similar to that developed by Sessler and West (ref. 23) with the exception that it is smaller in size and has an adjustable diaphragm tension. This additional feature in the transducer design was introduced by Carl Rumble of NASA Langley Research Center. The diaphragm of the transducer, both sides of which are exposed to the pressure field, is a permanently polarized dielectret foil made of 0.0037-cm metalized Mylar. The case is made of brass and is about 1.25 cm in diameter and 0.96 cm thick. The calibration is made in an impedance tube for frequency response, sensitivity, directivity, phase distortion, and harmonic distortion. The most reliable method of calibration is the one made in the impedance tube (fig. 24). Let the incident wave have an amplitude A and the reflected wave have an amplitude B. The pressure is given by

$$
\begin{aligned}
p(x,t) &= A\cos(\omega t - kx) + B\sin\left[\omega t + kx + \mu(\omega)\right] \\
&= \left\{A + B\cos\left[2kx + \mu(\omega)\right]\right\}\cos(\omega t - kx) - B\sin\left[2kx + \mu(\omega)\right]\sin(\omega t - kx)
\end{aligned}
\tag{B1}
$$

The root-mean-square pressure becomes

$$
\left[p(x)\right]_{rms} = \frac{1}{(2)^{1/2}}\left\{A^2 + B^2 + 2AB\cos\left[2kx + \mu(\omega)\right]\right\}^{1/2} \tag{B2}
$$

Then from equation (B1) the pressure gradient becomes

$$
\begin{aligned}
\frac{\partial p(x,t)}{\partial x} &= \frac{\omega}{c}A\sin(\omega t - kx) - \frac{\omega}{c}B\sin\left[\omega t + kx + \mu(\omega)\right] \\
&= \frac{\omega}{c}\left\{A - B\cos\left[2kx + \mu(\omega)\right]\right\}\sin(\omega t - kx) \\
&\quad - \frac{\omega}{c}B\sin\left[2kx - \mu(\omega)\right]\cos(\omega t - kx)
\end{aligned}
\tag{B3}
$$

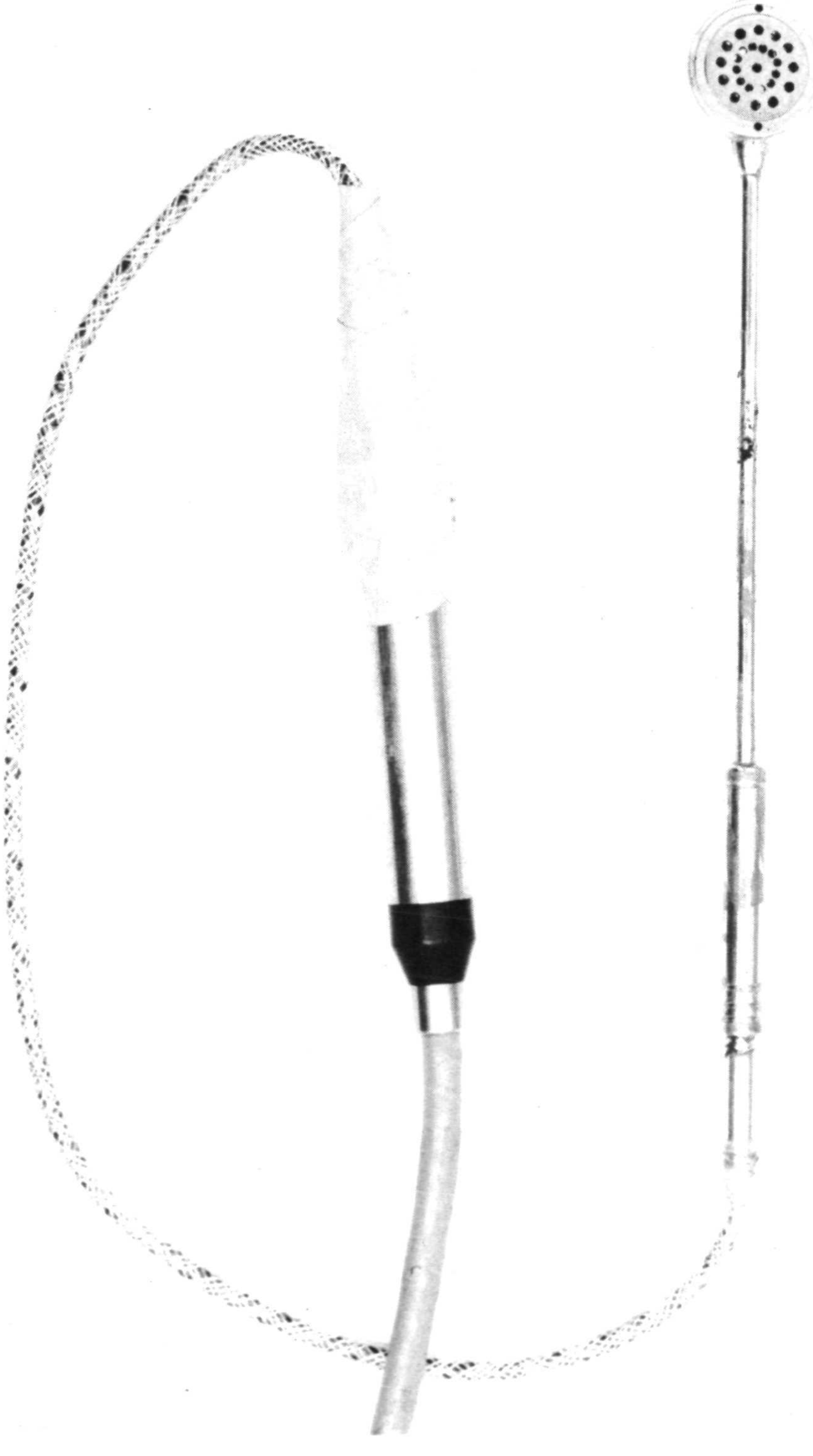

L-71-10 068

Figure 23.- Pressure gradient transducer.

L-73-3073

Figure 24.- Calibration of pressure gradient transducer.

and the root-mean-square pressure gradient can be written as

$$\left[\frac{\partial p(x)}{\partial x}\right]_{rms} = \frac{1}{(2)^{1/2}}\frac{\omega}{c}\left\{A^2 + B^2 + 2AB\cos\left[2kx + \mu(\omega)\right] - 4AB\cos\left[2kx + \mu(\omega)\right]\right\}^{1/2}$$

$$= \frac{\omega}{c}\left[p(x)\right]_{rms}\left\{1 - \frac{4AB\cos\left[2kx + \mu(\omega)\right]}{A^2 + B^2 + 2AB\cos\left[2kx + \mu(\omega)\right]}\right\}^{1/2}$$

$$= \frac{\omega}{c}\left[p(x)\right]_{rms}(1 + \epsilon) \tag{B4}$$

where $|\epsilon| \leqq \frac{2AB}{A^2 + B^2}$.

From equation (B4) the error ϵ made in the calibration of the pressure transducer depends on the amplitude of the standing-wave ratio. To minimize this error, the downstream end of the impedance tube was treated with an anechoic termination. Calculations show that for a standing-wave ratio of 0.25 dB, the amount of error introduced is of order $\epsilon = 3$ percent. The calibration was made for those frequencies in which the standing-wave ratio did not exceed this value.

The sensitivity is defined as

$$S(x,t) = K\frac{\partial p(x,t)}{\partial x}$$

and from equation (4)

$$K = \frac{S_{rms}}{\left(\frac{\partial p}{\partial x}\right)_{rms}}\frac{c}{\omega} \tag{B5}$$

The frequency-response calibration is made by placing the transducer in a spherical sound field generated by an artificial mouth. The response is shown in figure 25(a) where the curve is flat up to 3000 Hz. The transducer measured the component of the pressure gradient which is normal to the transducer face. This result is apparent in the figure where the sensitivity is seen to be down 3 dB when the gradient is incident at 45° to the face. The sensitivity factor K is plotted in figure 25(b); it remains constant up to a frequency of 3000 Hz. The phase-angle calibration was made by measuring the phase-angle difference between output voltage and incident pressure. The difference was within 3° from 200 to 3000 Hz. Furthermore, the harmonic distortion for an input pressure between 85 dB and 125 dB was linear within 5 percent.

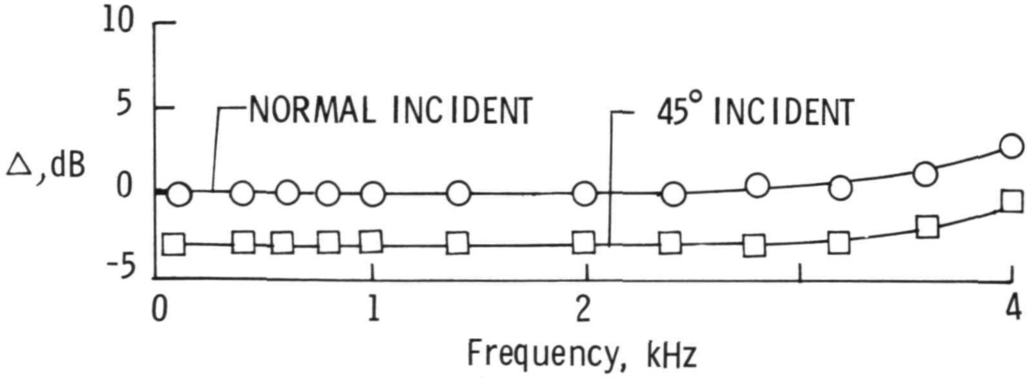

(a) Transducer frequency response.

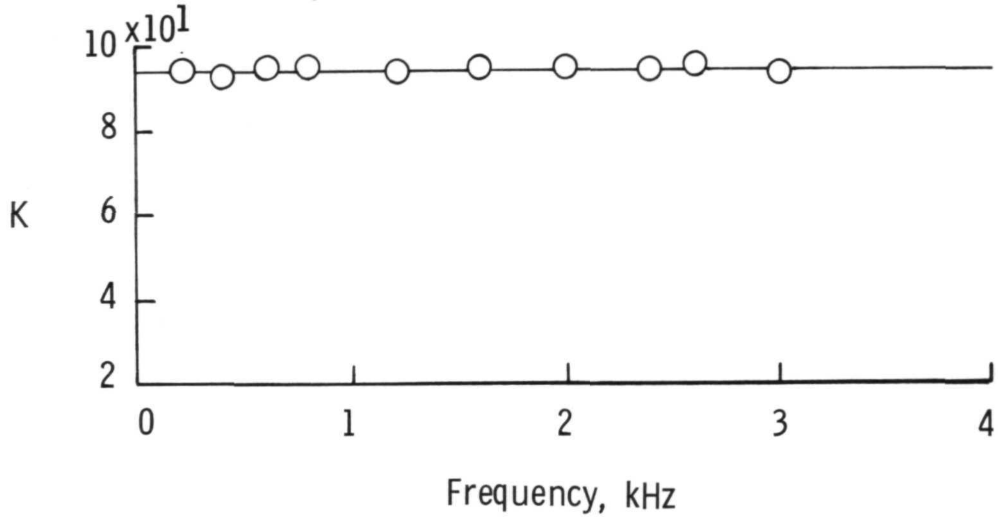

(b) Transducer sensitivity factor, K.

Figure 25.- Transducer calibration.

Since this measurement was made, further developments have taken place in improving the frequency response and the sensitivity of the transducer. Additional studies pertinent to the design of the pressure transducer in terms of the mechanical, acoustical, and electrical characteristic have been recently completed by E. Gonzaga (ref. 24).

REFERENCES

1. Lighthill, M. J.: On Sound Generated Aerodynamically. I. General Theory. Proc. Roy. Soc. (London), ser. A, vol. 211, no. 1107, Mar. 20, 1952, pp. 564-587.
2. Maestrello, L.; and McDaid, E.: Acoustic Characteristics of a High-Subsonic Jet. AIAA J., vol. 9, no. 6, June 1971, pp. 1058-1066.
3. Maestrello, L.; and McDaid, E.: Acoustic Characteristics of a High-Subsonic Jet. AIAA Paper No. 70-234, Jan. 1970.
4. Lilley, Geoffrey M.; Plumblee, Harry E.; Strahle, Warren C.; Ruo, Song-Yeong; and Doak, Philip E.: The Generation and Radiation of Supersonic Jet Noise. Vol. IV – Theory of Turbulence Generated Jet Noise, Noise Radiation From Upstream Sources, and Combustion Noise. AFAPL-TR-72-53, Vol. IV, U.S. Air Force, July 1972.
5. Doak, Philip E.: The Generation and Radiation of Supersonic Jet Noise. Vol. III – Progress Toward Unified Theory of Jet Engine Noise. AFAPL-TR-72-53, U.S. Air Force, July 1972.
6. Mollo-Christensen, Erik: Jet Noise and Shear Flow Instability Seen From an Experimenter's Viewpoint. Trans. ASME, Ser. E: J. Appl. Mech., vol. 34, no. 1, Mar. 1967, pp. 1-7.
7. Crow, S. C.; and Champagne, F. H.: Orderly Structure in Jet Turbulence. J. Fluid Mech., vol. 48, pt. 3, Aug. 16, 1971, pp. 547-591.
8. Hardin, Jay C.: Analysis of Noise Produced by an Orderly Structure of Turbulent Jets. NASA TN D-7242, 1973.
9. Lee, Hie K.; and Ribner, H. S.: Direct Correlation of Noise and Flow of a Jet. J. Acoust. Soc. Amer., vol. 52, no. 5 (pt. 1), Nov. 1972, pp. 1280-1290.
10. Phillips, O. M.: The Irrotational Motion Outside a Free Turbulent Boundary. Proc. Cambridge Phil. Soc., vol. 51, pt. 1, Jan. 1955, pp. 220-229.
11. Stewart, R. W.: Irrotational Motion Associated With Free Turbulent Flows. J. Fluid Mech., vol. 1, pt. 6, Dec. 1956, pp. 593-606.
12. Kibens, Valdis: The Intermittent Region of a Turbulent Boundary Layer. Ph. D. Diss., The Johns Hopkins Univ., 1968.
13. Bradbury, L. J. S.: The Structure of a Self-Preserving Turbulent Plane Jet. J. Fluid Mech., vol. 23, pt. 1, Sept. 1965, pp. 31-64.
14. Bradshaw, P.: Irrotational Fluctuations Near a Turbulent Boundary Layer. J. Fluid Mech., vol. 27, pt. 2, Feb. 2, 1967, pp. 209-230.

15. Morse, Philip M.; and Feshbach, Herman: Methods of Theoretical Physics. Pt. I, McGraw-Hill Book Co., Inc., 1953.

16. Atvars, J.; Schubert, L. K.; Grande, E.; and Ribner, H. S.: Refraction of Sound by Jet Flow or Jet Temperature. NASA CR-494, 1966.

17. Kock, W. E.; and Harvey, F. K.: A Photographic Method for Displaying Sound Wave and Microwave Space Patterns. Bell Systems Tech. J., vol. 30, no. 3, July 1951, pp. 564-587.

18. Rainey, James T.; and Neville, Donald G.: Sound Field Visualization Technique. Sound & Vibration, vol. 6, no. 12, Dec. 1972, pp. 10, 12, and 14.

19. Ribner, H. S.: On the Strength Distribution of Noise Sources Along a Jet. UTIA Rep. No. 51 (AFOSR TN-58-359, AD 154 264), Inst. Aerophys., Univ. of Toronto, Apr. 1958.

20. Powell, Alan: Similarity and Turbulent Jet Noise. J. Acoust. Soc. Amer., vol. 31, no. 6, June 1959, pp. 812-813.

21. Lilley, G. M.: On the Noise From Air Jets. Brit. A.R.C. 20,376, Sept. 8, 1958.

22. Lush, P. A.: Measurements of Subsonic Jet Noise and Comparison With Theory. J. Fluid Mech., vol. 46, pt. 3, Apr. 1971, pp. 477-500.

23. Sessler, G. M.; and West, J. E.: First-Order Gradient Microphone Based on the Foil-Electret Principle: Discrimination Against Air-Borne and Solid-Borne Noises. J. Acoust. Soc. Amer., vol. 46, no. 5 (pt. 1), Nov. 1969, pp. 1081-1086.

24. Gonzaga, Ernesto Agrular: On the Design of Pressure Gradient Condenser Microphone. M.S. Thesis, George Washington Univ., 1972.

NASA-Langley, 1973 —— 12 L-8871

> *"The aeronautical and space activities of the United States shall be conducted so as to contribute . . . to the expansion of human knowledge of phenomena in the atmosphere and space. The Administration shall provide for the widest practicable and appropriate dissemination of information concerning its activities and the results thereof."*
>
> —NATIONAL AERONAUTICS AND SPACE ACT OF 1958

NASA SCIENTIFIC AND TECHNICAL PUBLICATIONS

TECHNICAL REPORTS: Scientific and technical information considered important, complete, and a lasting contribution to existing knowledge.

TECHNICAL NOTES: Information less broad in scope but nevertheless of importance as a contribution to existing knowledge.

TECHNICAL MEMORANDUMS: Information receiving limited distribution because of preliminary data, security classification, or other reasons. Also includes conference proceedings with either limited or unlimited distribution.

CONTRACTOR REPORTS: Scientific and technical information generated under a NASA contract or grant and considered an important contribution to existing knowledge.

TECHNICAL TRANSLATIONS: Information published in a foreign language considered to merit NASA distribution in English.

SPECIAL PUBLICATIONS: Information derived from or of value to NASA activities. Publications include final reports of major projects, monographs, data compilations, handbooks, sourcebooks, and special bibliographies.

TECHNOLOGY UTILIZATION PUBLICATIONS: Information on technology used by NASA that may be of particular interest in commercial and other non-aerospace applications. Publications include Tech Briefs, Technology Utilization Reports and Technology Surveys.

Details on the availability of these publications may be obtained from:

SCIENTIFIC AND TECHNICAL INFORMATION OFFICE
NATIONAL AERONAUTICS AND SPACE ADMINISTRATION
Washington, D.C. 20546